Available online at www.sciencedirect.com

ScienceDirect

Procedia Engineering00 (2015) 000–000

Procedia Engineering

www.elsevier.com/locate/procedia

6th BSME International Conference on Thermal Engineering (ICTE 2014)

Effects of Thermal Diffusion on Viscoelastic Fluid Flow through a Vertical Flat Plate

Sheikh Imamul Hossain and Md. Mahmud Alam*

Mathematics Discipline, Khulna University, Khulna-9208, Bangladesh

Abstract

Viscoelastic fluid flow through a semi-infinite vertical rigid plate with diffusion-thermo and thermal-diffusion has been studied. To obtain the non-dimensional, coupled non-linear momentum, energy and concentration equations, the usual transformations have been used. The obtained non-dimensional equations have been solved by implicit finite difference technique. The stability and convergence analysis have been analyzed. From the above analysis, parameters restriction have been obtained to calculate the converge results. The effects of the various parameters entering into the problem on the velocity, temperature and concentration are shown graphically. Finally, a qualitative comparison with the published results is shown in tabular form.

Keywords: Viscoelastic fluid, diffusion-thermo, thermal-diffusion, implicit finite difference method;

© 2015 The Authors. Published by Elsevier Ltd.
Peer-review under responsibility of organizing committee of the 6th BSMEInternational Conference on Thermal Engineering (ICTE 2014).

1. Introduction

The viscoelastic fluid has been received momentum in the recent past because of its numerous applications in polymer technology, metallurgy, polymer sheet extrusion from a dye, polymer processing industry in particular in manufacturing process of artificial film. The study of boundary layer flow of a viscoelastic fluid through a vertical plate in the presence of Soret and Dufour's effect has wide range of applications in the field of chemical engineering

* Corresponding author. Tel.: +0-000-000-0000 ; fax: +0-000-000-0000 .
E-mail address: alam_mahmud2000@yahoo.com.

1877-7058 © 2015 The Authors. Published by Elsevier Ltd.
Peer-review under responsibility of organizing committee of the 6th BSME International Conference on Thermal Engineering (ICTE 2014).

and production of synthetic sheets. This is consequential to the production of heavy crude oils by means of thermal process. These oils considered as viscoelastic fluid which has both viscous and elastic property.

Diffusion occurs in a mixture under the presence of temperature gradients even when there are no concentration differences. This process is defined as the thermal-diffusion. In other words it can be said that the thermal-diffusion occurs when mass flux can be generated by a temperature gradient. This effect is also known as Soret effect.

Rajagopal et al. [1] studied the boundary layer flow of a viscoelastic fluid over a stretching sheet. However, Eckert and Drake [2] have showed many cases where Dufour effect cannot be neglected. In this regards, Tsai and Huang [3] investigated the heat and mass transfer for Soret and Dufour's effects on Hiemenz flow through porous medium onto a stretching surface. Recently Damseh and Shannak [4] analyzed that the Visco-elastic fluid flow past an infinite vertical porous plate in the presence of first-order chemical reaction. Sreekanth et al. [5] studied about hydromagnetic natural convection flow of an incompressible viscoelastic fluid between two infinite vertical moving and oscillating plates. Very recent Gbadeyan et al. [6], examined heat and mass transfer for Soret and Dufour's effect on mixed convection boundary layer flow over a stretching vertical surface in a porous medium filled with a viscoelastic fluid in the presence of magnetic field.

Our aim is to extend the work of Gbadeyan et al. [6] for unsteady case and to solve the problem by implicit finite difference method. In this paper, the work has been done with the effects of both thermal and mass diffusion on two dimensional unsteady flow of an incompressible viscoelastic fluid through a vertical plate.

2. Mathematical formulation

Consider the unsteady two-dimensional laminar flow of an incompressible viscoelastic fluid (obeying second grade model) through a vertical rigid plate with thermal-diffusion and diffusion thermo effects. The positive x coordinate is measured along the plate in the direction of fluid motion and the positive y coordinate is measured normal to the plate. The variable temperature T_w and variable concentration C_w at wall of the plate occupied with viscoelastic fluid of uniform ambient temperature T_∞ and uniform ambient concentration C_∞ also the uniform velocity U_0. The physical configuration of the above problem is given in Fig. 1.

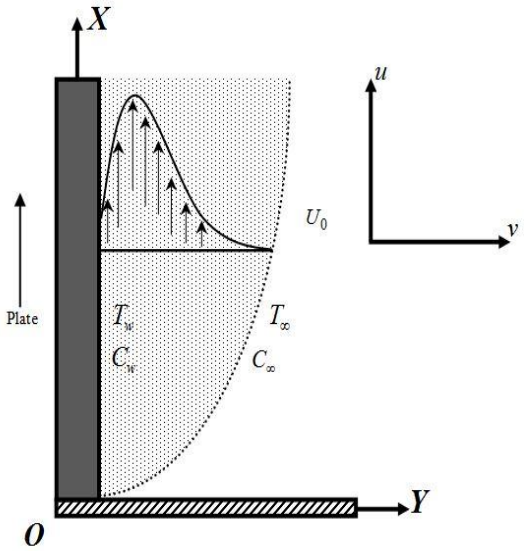

Fig.1. Physical configuration and coordinate system.

The following dimensionless variables that are used to obtained dimensionless governing equations (1)- (4) ;

$$X=\frac{xU_0}{\upsilon}, Y=\frac{yU_0}{\upsilon}, U=\frac{u}{U_0}, V=\frac{v}{U_0}, \tau=\frac{tU_0^2}{\upsilon}, \theta=\frac{T-T_\infty}{T_w-T_\infty},$$

$$\phi=\frac{C-C_\infty}{C_w-C_\infty}$$

Using these above dimensionless variables, the following dimensionless equations have been obtained as;

$$\frac{\partial U}{\partial X}+\frac{\partial V}{\partial Y}=0 \tag{1}$$

$$\frac{\partial U}{\partial \tau}+U\frac{\partial U}{\partial X}+V\frac{\partial U}{\partial Y}=G_r\theta+G_m\phi+\frac{\partial^2 U}{\partial Y^2}+K\left[\frac{\partial^3 U}{\partial \tau \partial Y^2}+U\frac{\partial^3 U}{\partial X\partial Y^2}+\frac{\partial U}{\partial X}\frac{\partial^2 U}{\partial Y^2}-\frac{\partial U}{\partial Y}\frac{\partial^2 V}{\partial Y^2}+V\frac{\partial^3 U}{\partial Y^3}\right] \tag{2}$$

$$\frac{\partial \theta}{\partial \tau}+U\frac{\partial \theta}{\partial X}+V\frac{\partial \theta}{\partial Y}=\frac{1}{P_r}\frac{\partial^2 \theta}{\partial Y^2}+D_u\frac{\partial^2 \phi}{\partial Y^2} \tag{3}$$

$$\therefore \frac{\partial \phi}{\partial \tau} + U\frac{\partial \phi}{\partial X} + V\frac{\partial \phi}{\partial Y} = \frac{1}{S_c}\frac{\partial^2 \phi}{\partial Y^2} + S_r\frac{\partial^2 \theta}{\partial Y^2} \tag{4}$$

The corresponding non-dimensional boundary conditions are as;

$$\begin{aligned} &\tau \succ 0, \quad U = 1, \quad V = 0, \quad \theta = 1, \quad \phi = 1, \text{ at } \quad Y = 0 \\ &\qquad\quad U = 0, \quad V = 0, \quad \theta \to 0, \quad \phi \to 0, \text{ as } \quad Y \to \infty \end{aligned} \tag{5}$$

The non-dimensional parameters are; Grashof number G_r , Modified Grashof number G_m , Viscoelastic parameter K , Prandtl number P_r , Dufour number D_u , Schmidt number S_c and Soret number S_r .

3. Shear Stress, Nusselt and Sherwood Number

From the velocity, the effects of various parameters on the local and average shear stress have been calculated. The following equations represent the local and average shear stress at the plate. Local shear stress $\tau_L = \mu\left(\frac{\partial u}{\partial y}\right)_{y=0}$ and average shear stress $\tau_A = \mu\int\left(\frac{\partial u}{\partial y}\right)_{y=0} dx$ which are proportional to $\left(\frac{\partial U}{\partial Y}\right)_{Y=0}$ and $\int_0^{100}\left(\frac{\partial U}{\partial Y}\right)_{Y=0} dX$ respectively. From the temperature field, the effects of various parameters on the local and average heat transfer coefficients have been investigated. The following equations represent the local and average heat transfer rate that is well known Nusselt number. Local Nusselt number, $N_{uL} = \mu\left(-\frac{\partial T}{\partial y}\right)_{y=0}$ and Average Nusselt number, $N_{uL} = \mu\int\left(-\frac{\partial T}{\partial y}\right)_{y=0} dx$ which are proportional to $\left(-\frac{\partial \theta}{\partial Y}\right)_{Y=0}$ and $\int_0^{100}\left(-\frac{\partial \theta}{\partial Y}\right)_{Y=0} dX$ respectively. From the concentration field, the effects of various parameters on the local and average mass transfer coefficients have been analyzed. The following equations represent the local and average mass transfer rate that is well known Sherwood number. Local Sherwood number, $S_{hL} = \mu\left(-\frac{\partial C}{\partial y}\right)_{y=0}$ and Average Sherwood number, $S_{hL} = \mu\int\left(-\frac{\partial C}{\partial y}\right)_{y=0} dx$ which are proportional to $\left(-\frac{\partial \phi}{\partial Y}\right)_{Y=0}$ and $\int_0^{100}\left(-\frac{\partial \phi}{\partial Y}\right)_{Y=0} dX$ respectively.

4. Numerical Analysis

To solve the non-dimension system by implicit finite difference technique, it is required a set of finite difference equations. In this case, the region within the boundary layer is divided by some mash of lines parallel to X and Y axes where $X-$axis is taken along the plate and $Y-$axis is normal to the plate as shown in Fig. 2. Here, the plate of height $X_{\max} = (100)$ i.e. X varies from 0 to 100 and it is assumed that the maximum length of boundary layer is $Y_{\max} = (35)$ as corresponding to $Y \to \infty$ i.e. Y varies from 0 to 35 have been considered. Consider $m = 125$ and $n = 125$ in X and Y directions. It is assumed that ΔX , ΔY are constant mesh sizes along X and Y directions respectively and taken as follows, $\Delta X = 0.8(0 \le x \le 100)$; $\Delta Y = 0.28(0 \le y \le 35)$ with the smaller time-step, $\Delta\tau = 0.005$.

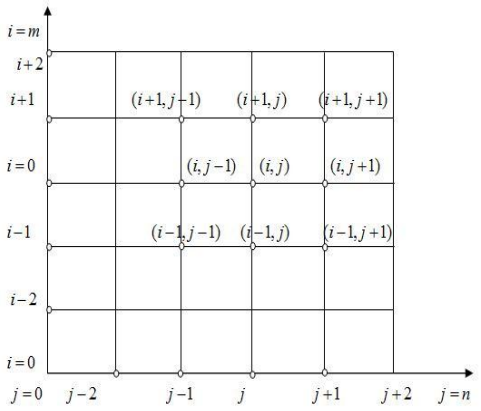

Fig. 2. Implicit finite difference system grid.

Let U', V', θ' and ϕ' denote the values of U, V, θ and ϕ at the end of a time-step respectively. An appropriate set of finite difference equations have been obtained as;

$$\frac{U'_{i,j}-U'_{i-1,j}}{\Delta X}+\frac{V'_{i,j}-V'_{i,j-1}}{\Delta Y}=0 \tag{6}$$

$$\frac{U'_{i,j}-U_{i,j}}{\Delta\tau}+U_{i,j}\frac{U_{i,j}-U_{i-1,j}}{\Delta X}+V_{i,j}\frac{U_{i,j+1}-U_{i,j}}{\Delta Y}=G_r\theta'_{i,j}+G_m\phi'_{i,j}+\frac{U_{i,j+1}-2U_{i,j}+U_{i,j-1}}{(\Delta Y)^2}$$
$$+K\left[\frac{U'_{i,j+1}-2U'_{i,j}+U'_{i,j-1}-U_{i,j+1}+2U_{i,j}-U_{i,j-1}}{\Delta\tau(\Delta Y)^2}\right.$$
$$+U_{i,j}\frac{U_{i,j+1}-2U_{i,j}+U_{i,j-1}-U_{i-1,j+1}+2U_{i-1,j}-U_{i-1,j-1}}{\Delta X(\Delta Y)^2}+V_{i,j}\frac{U_{i,j+2}-3U_{i,j+1}+3U_{i,j}-U_{i,j-1}}{(\Delta Y)^3}$$
$$\left.+\frac{U_{i,j}-U_{i-1,j}}{\Delta X}\frac{U_{i,j+1}-2U_{i,j}+U_{i,j-1}}{(\Delta Y)^2}-\frac{U_{i,j+1}-U_{i,j}}{\Delta Y}\frac{V_{i,j+1}-2V_{i,j}+V_{i,j-1}}{(\Delta Y)^2}\right] \tag{7}$$

$$\frac{\theta'_{i,j}-\theta_{i,j}}{\Delta\tau}+U_{i,j}\frac{\theta_{i,j}-\theta_{i-1,j}}{\Delta X}+V_{i,j}\frac{\theta_{i,j+1}-\theta_{i,j}}{\Delta Y}=\frac{1}{P_r}\frac{\theta_{i,j+1}-2\theta_{i,j}+\theta_{i,j-1}}{(\Delta Y)^2}+D_u\frac{\phi_{i,j+1}-2\phi_{i,j}+\phi_{i,j-1}}{(\Delta Y)^2} \tag{8}$$

$$\frac{\phi'_{i,j}-\phi_{i,j}}{\Delta\tau}+U_{i,j}\frac{\phi_{i,j}-\phi_{i-1,j}}{\Delta X}+V_{i,j}\frac{\phi_{i,j+1}-\phi_{i,j}}{\Delta Y}=\frac{1}{S_c}\frac{\phi_{i,j+1}-2\phi_{i,j}+\phi_{i,j-1}}{(\Delta Y)^2}+S_r\frac{\theta_{i,j+1}-2\theta_{i,j}+\theta_{i,j-1}}{(\Delta Y)^2} \tag{9}$$

with initial and boundary conditions;

$U^n_{i,0}=1, V^n_{i,0}=0, \theta^n_{i,0}=1, \phi^n_{i,0}=1$

(10)

$U^n_{i,L}=0, V^n_{i,L}=0, \theta^n_{i,L}=0, \phi^n_{i,L}=0$ where $L\to\infty$.

Here the subscripts *i* and *j* designate the grid points with *X* and *Y* coordinates respectively and the subscript n represents a value of time, $\tau=n\Delta\tau$ where $n=0,1,2,3,\ldots\ldots\ldots$ The new velocity U', the new temperature θ' and the new concentration ϕ' at all interior nodal points may be obtained by successive applications of above finite difference equations. The numerical values of the local Shear Stress, Nusselt number and Sherwood number are evaluated by five-point approximate formula for the derivatives and then the average Shear Stress, Current density, Nusselt number and Sherwood number are calculated by the use of the **Simpson's** $\frac{1}{3}$ integration formula.

The stability conditions of the problem are as furnished below as;

$$U\frac{\Delta\tau}{\Delta X}+|V|\frac{\Delta\tau}{\Delta Y}+\frac{2}{P_r}\frac{\Delta\tau}{(\Delta Y)^2}\le 1 \text{ and } U\frac{\Delta\tau}{\Delta X}+|V|\frac{\Delta\tau}{\Delta Y}+\frac{2}{S_c}\frac{\Delta\tau}{(\Delta Y)^2}\le 1$$

When $\Delta\tau$ and ΔY approach to zero then the problem will be converged. The convergence criteria of the problem are $P_r\ge 0.13$ and $S_c\ge 0.13$.

5. RESULTS AND DISCUSSION

To obtain the steady-state solutions, the computations have been carried out up to dimensionless time $\tau=80$. The results of the computations, however, show little changes in the above mentioned quantities after dimensionless time $\tau=60$. Thus the solutions for dimensionless time $\tau=60$ are essentially steady-state solutions. To observe the physical situation of the problem, the steady-state solutions have been illustrated in Figs. 3-7.

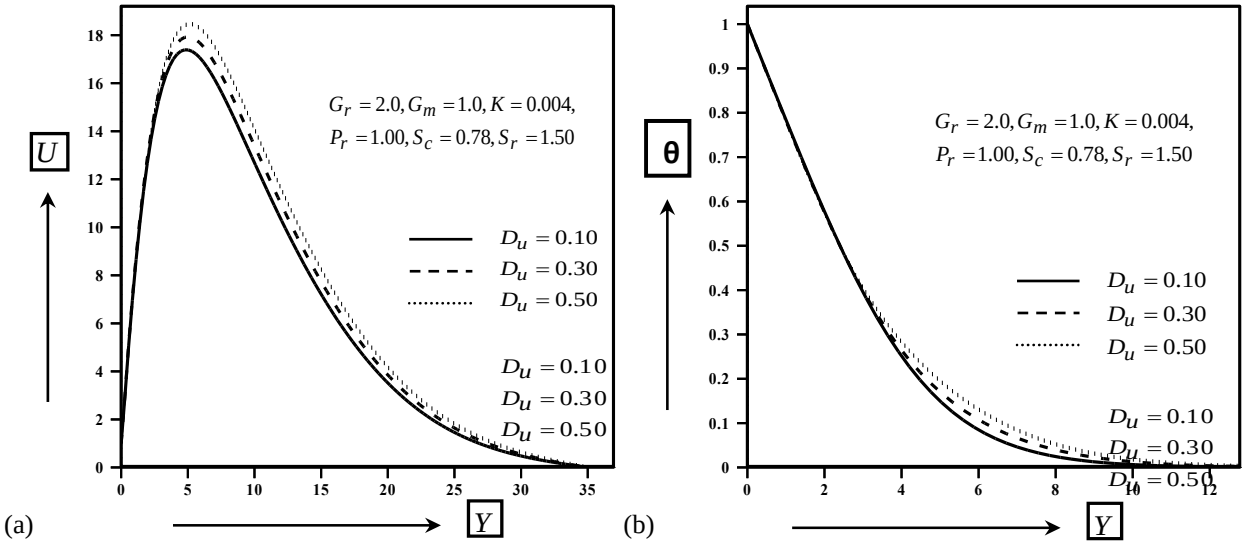

Figs.3 (a) Velocity distributions and (b) Temperature distributions for different values of Dufour number.

The velocity and temperature distributions have been shown in Figs. 3(a) and 3(b) for different values of Dufour number D_u . Both the velocity and temperature distributions increase with the increase of Dufour number D_u . The temperature distributions have been shown in Figs. 4(a) and 4(b) for different values of Viscoelastic parameter K and Prandtl number P_r respectively. In both cases the thermal boundary layers have been decreased with the increase of Viscoelastic parameter K and Prandtl number P_r .

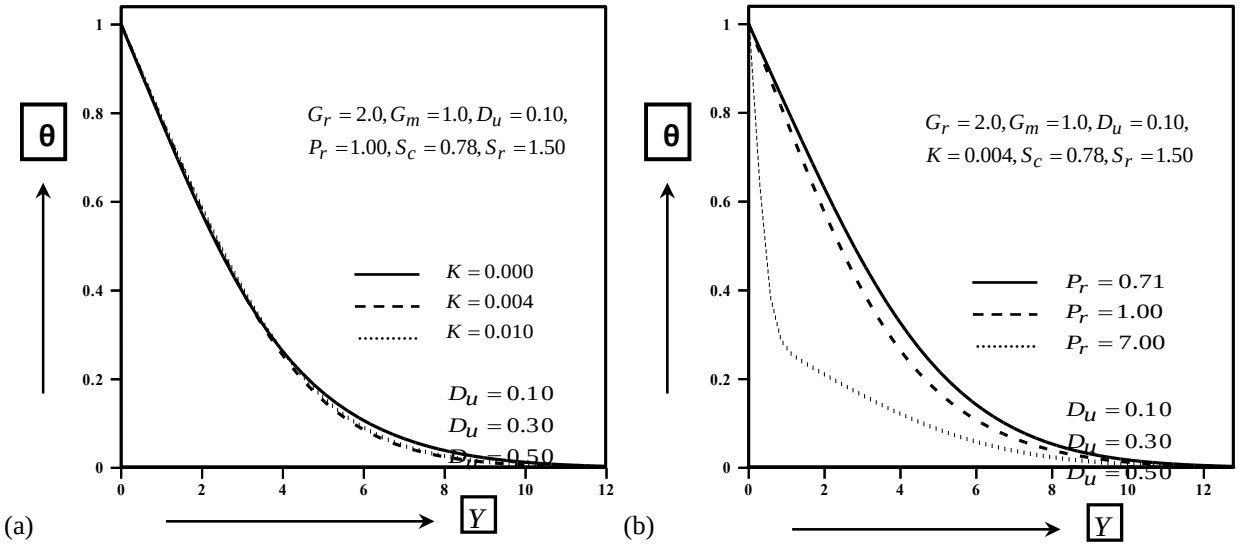

Figs.4 (a) Temperature distributions of for different values of Viscoelastic parameter and (b) Temperature distributions for different values of Prandtl number.

The Concentration distributions have been shown in Figs. 5(a) and 5(b) for different values of Dufour number D_u and Soret number S_r respectively. The concentration distributions decreases with the increase of Dufour number D_u while increases with the increase of Soret number S_r .

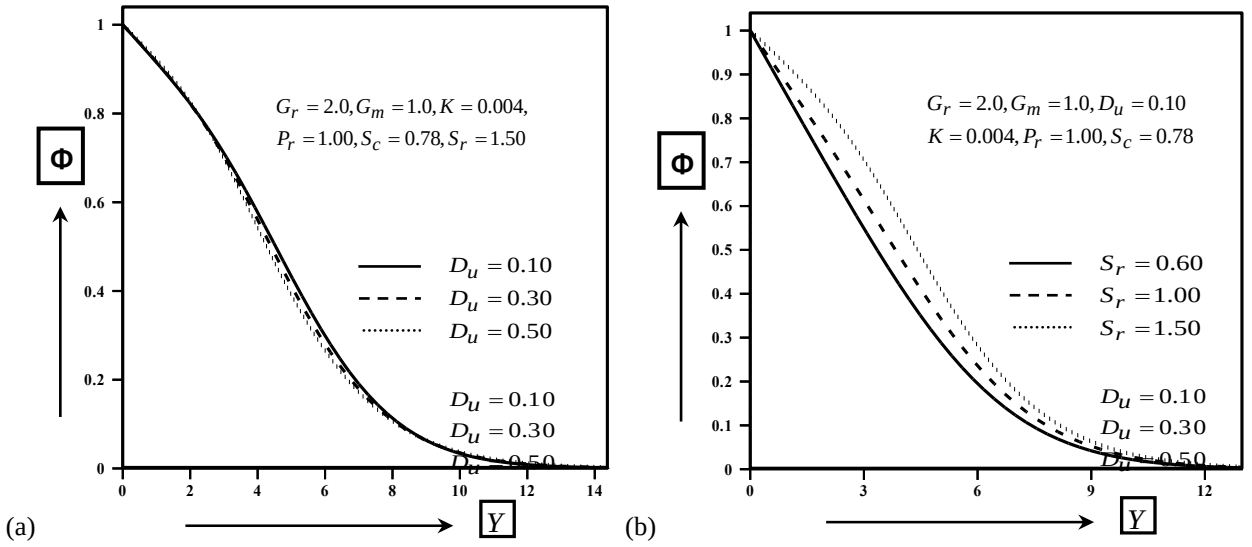

Figs.5 (a) Concentration distributions of for different values of Dufour number and (b) Concentration distributions for different values of Soret number.

The Shear stress for different values of Prandtl number P_r have been plotted graphically in Figs. 6(a). The Shear stress decreases with the rise of Prandtl number P_r. The Nusselt number for different values of Soret number S_r have been plotted in Fig. 6(b) and the Nusselt number decreases with the increase of Soret number S_r.

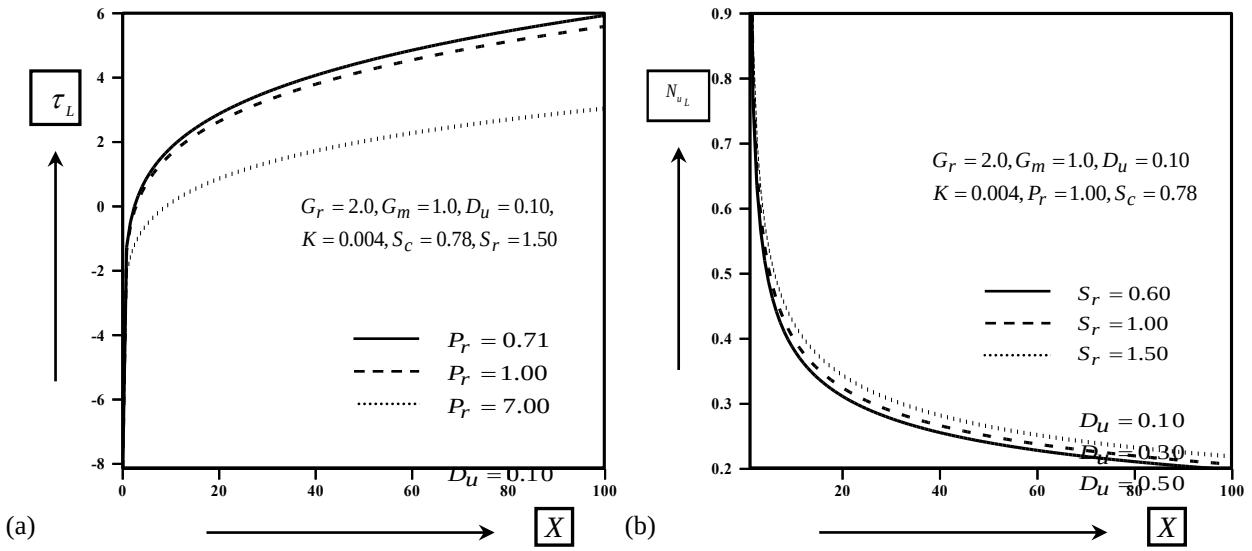

Figs.6 (a) Shear stress for different values of Prandtl number and (b) Nusselt number for different values of Soret number.

The Sherwood number has been shown in Figs. 7(a) and 7(b) for different values of Grashof number G_r and Schmidt number S_c. The Sherwood number increases with the increase of Grashof number G_r while decreases with the increase of Schmidt number S_c.

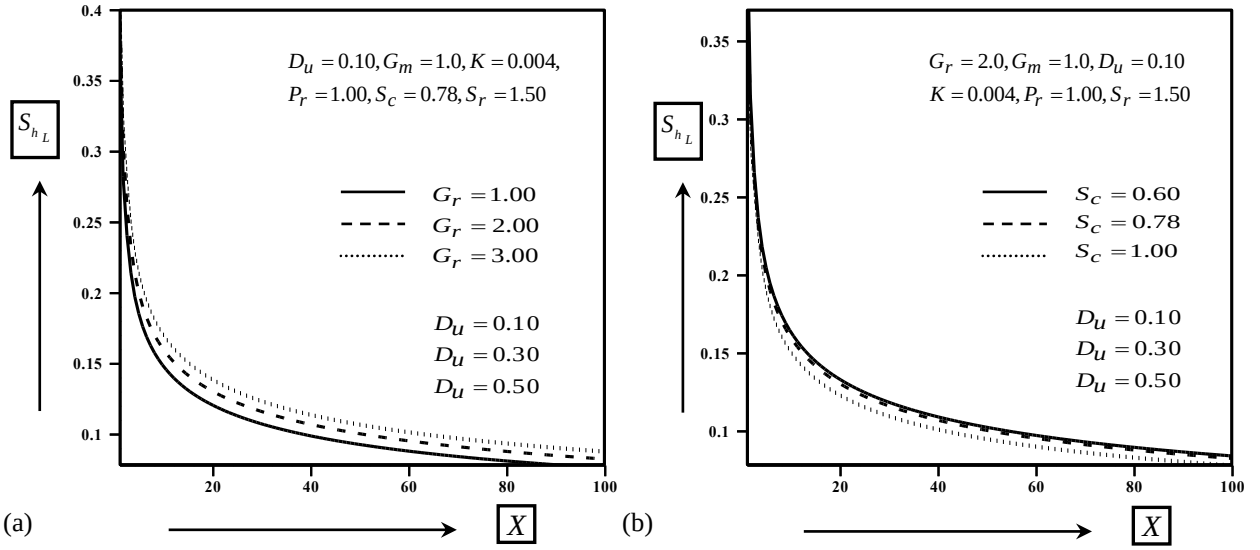

Figs.7 (a) Sherwood number for different values of Grashof number and (b) Sherwood number for different values of Schmidt number.

Finally, a qualitative comparison of the present steady-state results with the published results (Gbadeyan et al. [6]) is presented in table 1. The accuracy of the present results is qualitatively as well as quantitatively good in case of all the flow parameters.

Table 1.Qualalitive comparison of the present results with the previous results

Increased Parameter	Pervious results given by Gbadeyan et al. [6]			Present results		
	$F'(\eta)$	$\theta(\eta)$	$\phi(\eta)$	U	θ	ϕ
D_u	Inc.	Inc.	Dec	Inc.	Inc.	Dec.
K		Dec.			Dec.	
P_r		Dec.			Dec.	
S_r			Inc.			Inc.

6. Conclusion

In this research work, the implicit finite difference solution of unsteady two-dimensional laminar flow of an incompressible viscoelastic fluid through a vertical plate with Soret and Dufour's effects has been studied. The physical properties are discussed for different values of various parameters and the accuracy of our results is qualitatively good in case of all the flow parameters. Some important findings of this study are given below;

1. For the increase of Dufour number D_u , the velocity, temperature distributions have been increased.
2. Temperature distributions have been decreased with the increase of Viscoelastic parameter K and Prandtl number P_r .
3. Concentration distributions have been decreased with the increase of Dufour number D_u .
4. Concentration distributions have been increased with Soret number S_r .
5. Shear stress has been decreased with the increase of Prandtl number P_r .
6. Nusselt number has been increased with the increase of Soret number S_r .
7. Sherwood number has been increased with the increase of Grashof number G_r while decreased for the increase of Schmidt number S_c .

References

[1] K. R. Rajagopal, T. Y. Na, A. S. Gupta, Flow of a viscoelastic fluid over a stretching sheet, Rheol. Acta. Vol. 23, 1984, pp 213-215.
[2] Eckert ER, Drake RM., Analysis of heat and mass transfer, McGraw Hill, New York, 1972.
[3] R. Tsai, J. S. Huang, Heat and mass transfer for Soret and Dufour's effects on Hiemenz flow through porous medium onto a stretching surface, int. j. Heat Mass Transfer. vol. 52, 2009, pp2399-2406.
[4] R. A. Damseh and B.A. Shannak, Visco-elastic fluid flow past an infinite vertical porous plate in the presence of first-order chemical reaction , Appl. Math. Mech. -Engl. Ed. vol. 31(8), 2010, pp955–962.
[5] S.Sreekanth, S. Venkataramana, G. Sreedhar Rao and R. Saravana, Hydromagnetic natural convection flow of an incompressible viscoelastic fluid between two infinite vertical moving and oscillating plates, Adv. Appl. Sci. Res., vol. 2(5),2011, pp185-196.
[6] Gbadeyan, J.A., Idowu, A.S., Ogunsola, A.W., Agboola, O.O., Olanrewaju, P.O., Heat and mass transfer for Soret and Dufour's effect on mixed convection boundary layer flow over a stretching vertical surface in a porous medium filled with a viscoelastic fluid in the presence of magnetic field, Global Journal of science Frontier Research, vol. 11(8), 2011, pp96-114.

Available online at www.sciencedirect.com

SciVerse ScienceDirect

Procedia Engineering00 (2015) 000–000

Procedia Engineering

www.elsevier.com/locate/procedia

6th BSME International Conference on Thermal Engineering (ICTE 2014)

Aerodynamic study of FIFA-approved footballs

Firoz Alam, Harun Chowdhury*, Israt Mustary and Bavin Loganathan

School of Aerospace, Mechanical and Manufacturing Engineering, RMIT University, Melbourne, 3083, Australia

Abstract

The game of football is world's most viewed, played and loved sport. Due to increasing technological advancements and demand for performance, the ball manufacturers have been developing new designs progressively since its inception over 100 years ago. A traditional spherical football made of 32 leather panels stitched together in 1970s has become 14 synthetic curved panels thermally bonded without stitches in 2006 and more recently 8 panels thermally bonded in 2010, and again some new designed balls in 2013. Despite being most popular game in the world, no data is available on aerodynamic properties of recently FIFA approved Adidas Cafusa (thermally bonded 32 panels), Nike Maxim (stitched 32 panels), Umbro Neo 2 Pro (stitched 14 panels, and Mitre Ultimax (stitched 26 panels) footballs. Hence the primary objectives of this study are to evaluate aerodynamic performance of these recently introduced balls and compare their aerodynamic properties. The aerodynamic forces and moments are measured experimentally for a range of wind speeds in wind tunnel. A field trial using professional players has also been undertaken. The aerodynamic forces and their non-dimensional coefficients were determined and compared. The player's perception was also discussed.

© 2015 The Authors. Published by Elsevier Ltd.
Peer-review under responsibility of organizing committee of the 6th BSME International Conference on Thermal Engineering (ICTE 2014).

Keywords: football; FIFA; drag; wind tunnel; field trial; flow visualisation.

* Corresponding author. Tel.: +61 3 99256103; fax: +61 3 99256108.
E-mail address: harun.chowdhury@rmit.edu.au

1877-7058 © 2015 The Authors. Published by Elsevier Ltd.
Peer-review under responsibility of organizing committee of the 6th BSME International Conference on Thermal Engineering (ICTE 2014).

1. Introduction

The football game is a truly world game with billions of audiences. The centre piece of the game is the spherical ball. The flight trajectory of a football ball is influenced by its aerodynamic characteristics. Depending on aerodynamic behavior, the ball can be deviated from the anticipated flight path resulting in an unpredictable flight trajectory. Lateral deflection in flight, commonly known as swing or knuckle, is well recognized in other spherical ball games such as cricket, baseball, golf, tennis and volleyball. Therefore, the aerodynamic properties of a football are considered to be considered fundamental for understanding the flight trajectory. It is true that a football among all other spherical sport balls is more balanced. Since 1970s, the design of footballs has undergone a series of technological changes utilizing new designs and manufacturing processes. Adidas, the official supplier of footballs to FIFA has applied thermal bonding replacing traditional stitching to make a seamless surface design by using 8 curved panels instead of 32 panels in its 2010 FIFA World Cup ball. The surface structure (texture, grooves, ridges, seams, etc) of the ball has also been altered in the process. In 2013, the same company introduced Cafusa 32 panels ball which thermally bonded without using traditional pentagon and hexagon panels. Two other balls namely Umbro Neo 2 Pro (stitched 14 panels), and Mitre Ultimax (stitched 26 panels) were introduced in 2012 and 2013 Although the aerodynamic behavior of other sports balls have been studied by Alam et al. [1], Mehta et al. [2] and Smits and Ogg [3], little information is available about the aerodynamic behavior of new footballs except the experiential studies by Alam et al. [4] and Asai and Kamemoto [5]. Studies by Goff and Carre [6] and Barber et al. [7, 10] provided some insights about the effect of surface structure of 32 panels balls however, no such data is available for new generation footballs introduced in 2012 and 2013. Therefore, the primary objective of this work is to experimentally study the aerodynamic properties of several soccer balls made of 32, 14, 26, & 8 leather and synthetic panels.

Nomenclature

F_D	aerodynamic drag (N)
C_D	aerodynamic drag coefficient
Re	Reynolds number
V	wind velocity (m/s)
μ	absolute dynamic viscosity of wind (Pa)
ρ	air density (kg/m^3)
A	projected frontal area of ball (m^2)
d	ball diameter (m)

2. Methodology

2.1. Description of soccer balls

Four new balls were selected for this study. They are: (a) 32 panels Adidas Cafusa, (b) 32 panels Nike Maxim, (c) 14 Panels Umbro Neo 2 Pro and (d) 26 panels Mitre Ultimax. The Cafusa ball was made by Adidas, Maxim by Nike, Neo by Umbro and Ultimax by Mitre. The Adidas Cafusa ball's panels are thermally bonded whereas the panels of other 3 balls are stitched together. The panels of Adidas Cafusa are traditional pentagons and hexagons. Similarly, the panels of Mitre ball have had complex shapes. The other two balls have traditional pentagon and hexagon panels. A pictorial view and the surface morphology of four balls are shown in Fig. 1. All four balls are FIFA approved.

Fig. 1. footballs with various panel and surface configurations.

2.2. Experimental setup

RMIT Industrial Wind Tunnel was selected for this study. The tunnel is a closed return circuit wind tunnel with a maximum speed of approximately 150 km/h. The rectangular test section's dimension is 3 m (wide) × 2 m (high) × 9 m (long), and is equipped with a turntable to yaw the model. Each ball was mounted on a six component force sensor (type JR-3) as shown in Fig. 2, and purpose made computer software was used to digitize and record all 3 forces (drag, side and lift forces) and 3 moments (yaw, pitch and roll moments) simultaneously. More details about the tunnel and its flow conditions can be found in Alam et al. [8]. A strut support was developed to hold the ball on a force sensor in the wind tunnel, and the schematic of experimental setup with a strut support is shown in Fig. 2. The aerodynamic effect of the strut support was subtracted from the mount with the ball. The distance between the bottom edge of the ball and the tunnel floor was 300 mm, which is well above the tunnel boundary layer and considered to be out of significant ground effect.

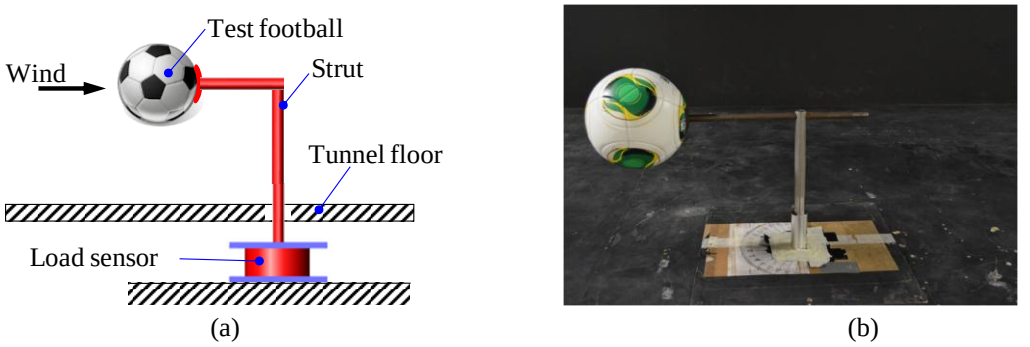

Fig. 2. (a) schematic of the experimental setup; (b) setup inside RMIT Industrial Wind Tunnel.

The aerodynamic drag coefficient (C_D) and the Reynolds number (Re) are defined as:

$$C_D = \frac{D}{\frac{1}{2}\rho V^2 A} \tag{1}$$

$$Re = \frac{\rho V d}{\mu} \tag{2}$$

The lift and side forces and their coefficients were not determined and presented in this paper. Only drag data is presented here.

3. Results and discussion

3.1. Wind tunnel measurements

Each ball as well as a sphere was tested at 20 to 100 km/h with an increment of 10 km/h. The aerodynamic drag was converted to non-dimensional parameter (drag coefficient, C_D). The sphere was made of foam and possesses slight roughness. The influence of the support on the ball was checked and found to be negligible. The repeatability of the measured forces was within ±0.01 N and the wind velocity was less than 0.027 m/s (e.g. 0.1 km/h). The C_D variations with Reynolds numbers for all balls and a foam-made sphere are shown in Fig 3. The flow transition for the sphere (not fully smooth) was noted at approximately $Re = 1.00 \times 10^5$ which agreed well with the published data [9].

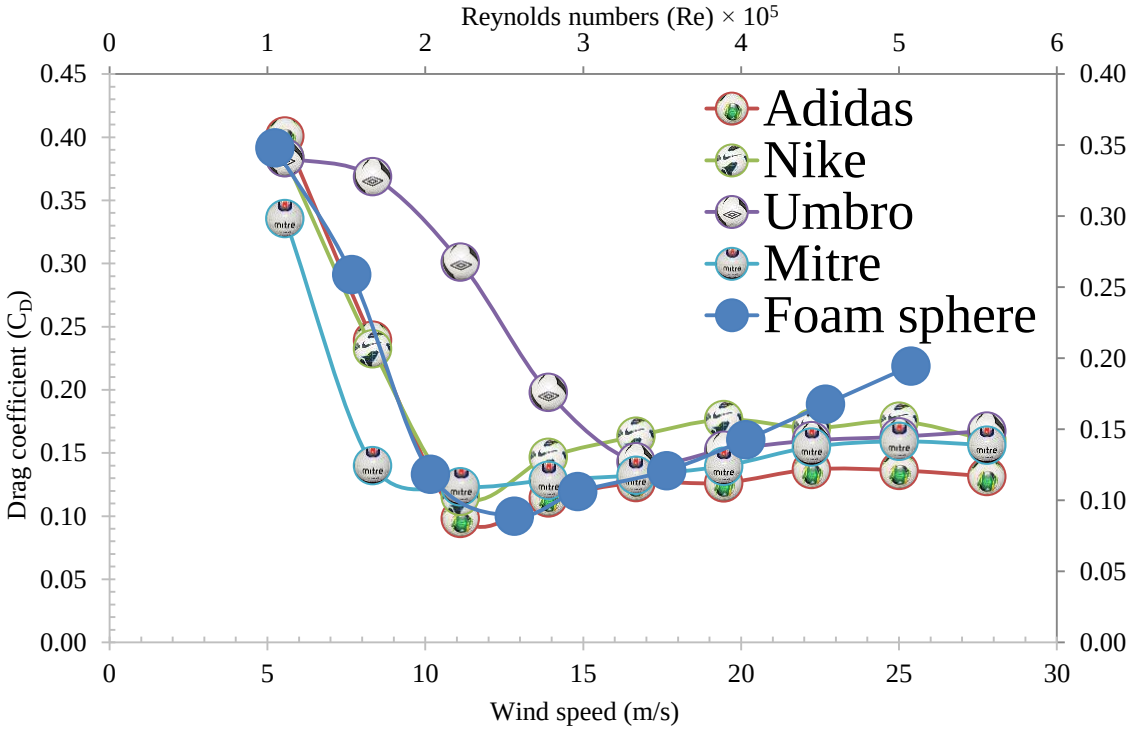

Fig. 3. C_D variation with Reynolds number for all six balls and a sphere.

The airflow reached supercritical Reynolds number at approximately 3.50×10^5. The critical Reynolds number for the Mitre (complex shaped 18 panels & stitched) ball occurs at 2.03×10^5 at which the drag coefficient is around 0.12. The flow transition from laminar to fully turbulent occurs between 5 and 20 m/s (~ 20-70 km/h). The Adidas Cafusa (32 panels contain no pentagons & hexagons, no stitches but thermally bonded) begins transition shortly before at $Re = 1.00 \times 10^5$ and becomes fully turbulent at 3.00×10^5. The drag coefficient at the beginning of the transition is about 0.40 while in the turbulent region it is initially 0.10 before rising to 0.15. Transition occurs between 5 and 15 m/s (20 - 50 km/h). The critical Reynolds number for Nike ball (32 pentagon and hexagon panels and are stitched together) occurs at about 2.03×10^5 at a drag coefficient of 0.12. The drag coefficient is around 0.18 in the fully turbulent flow regime. The Ambro ball with 32 pentagon and hexagon panels and stitches undergoes flow transition between $Re = 1.15 \times 10^5$ and $Re = 1.40 \times 10^5$. The flow transition for occurs much later due to its relatively smooth surface compared to all other balls and the foam-made sphere. The critical Reynolds number occurs at $Re = 1.30 \times 10^5$ and the flow is fully turbulent after $Re = 3.40 \times 10^5$. The drag coefficient at the beginning of transition is 0.40, 0.14 at the supercritical transition and 0.16 at the end of transition (transcritical). It is worthwhile to mention that the C_D value for the foam-made sphere with rough surface is 0.40 at the beginning of the

flow transition, 0.09 at super critical transition and 0.2 at transcritical transition. The flow transitional behaviour of Adidas Cafusa, Nike Maxim and the foam-made sphere is very similar. The Mitre ball constitutes the roughest surface due its complex panel design and stitches and experiences the flow transition earlier than all other balls and the sphere tested. The surface with Umbro Neo ball is the smoothest with its 32 pentagon and hexagon panels that are stitched together allows the flow transition much later than all other balls and the foam-made sphere as shown in Fig. 3.

3.2. In-field measurements

The primary objective of the field measurements was to explore the player's feel and the correlation with the wind tunnel data if any. The filed tests were conducted over two days, at ideal day and night conditions on a relatively wet surface (the ideal playing conditions). Five elite level (State premium divisional professional) players were selected for this study. Tests were undertaken with following characteristics: each ball was tested after each other with the same player so that they can express their opinions on each ball accordingly. The first test was a penalty kick. The test was done by each player, and they were instructed to kick each ball the same way. The players then rated each ball out of 5. The second test was a free kick from the edge of the 18 yards box. The players were advised to kick each ball consistently, either to place the ball or to go for power, then rate each ball out of 5. The third test was a corner. The players were told to aim for the penalty spot, and they had to kick each ball consistently. Each player then rated the behaviour of the ball at a scale of 1 to 5. The fourth test was a kick from the half way line. The objective of this kick was to see the distance each ball travels. The players were under instruction to kick the ball as hard as they could. Each player then rated the balls out of 5. The final test was a goal kick from the edge of the 6 yards box. This was to see the trajectory of the ball. The players again were instructed to kick it has hard as they could. After the kick, the players rated the balls out of 5. Later, they had an in-game situation test where they played with each ball for 30 seconds and determine the better ball in a match game situation.

The findings of the field measurements showed that the Umbro Neo 2 Pro was the most consistent ball to play with; each player rated it in the top two, with either Adidas Cafusaor Nike Maxim in other slot. The reason for the Umbro Neo being preferred to instead of other balls is due to its 14-panel structure and its under layer foam design. Weight tests done on the balls also concluded that Umbro was the lightest ball with Adidas being the heaviest. The tests incorporated every phase of the game.

4. Concluding remarks

The reduced seam lengths and increasing surface smoothness reduces drag coefficient at high Reynolds number (high speeds). At higher speeds, the Adidas Cafusa maintains a lower drag coefficient than all other balls it possesses less surface disturbances due to thermal bonding instead of stitches. Although transitional flow occurred at same velocity for Adidas Cafusa and Nike Maxim, the Cafusa experienced a lower drag coefficient at transcritical stage of the turbulent flow. The Mitre Ultimax due to its complex surface roughness has the lowest drag coefficient prior to the super critical transition. However, it also displays the similar behaviour to that of the Cafusa ball after supercritical and transcritical regions. The Umbro Neo undergoes flow transition at higher Reynolds number compared to all other ball which is believed to due to its relatively smooth surface compared to other balls.

The perception of players indicates that Umbro Neo 2 ball is most consistent in terms of player's anticipated target. The ball is preferred practice ball by the players. However, most players prefer Adidas Cafusa and Nike Maxim as match balls due to easier control and better stability. Further aerodynamic investigations are underway to determine the aerodynamic stability of these balls.

References

[1] F. Alam, H. Chowdhury, M. Stemmer, Z. Wang, J. Yang, Effects of surface structure on soccer ball aerodynamics, Procedia Engineering. 34 (2012) 146-151.

[2] R. D. Mehta, F. Alam, A. Subic, Aerodynamics of tennis balls- a review, Sports Technology. 1(1) (2008) 1-10.

[3] A.J. Smits, S. Ogg, Golf ball aerodynamics, The Engineering of Sport 5. 1 (2004) 3-12.

[4] F. Alam, H. Chowdhury, H. Moria, , F.K. Fuss, I. Khan, F. Aldawi, A. Subic, Aerodynamics of contemporary FIFA soccer balls, Procedia Engineering. 13 (2011)188-193.
[5] T. Asai, K. Kamemoto, Flow structure of knuckling effect in footballs, Fluids and Structures. 27(5-6) (2011) 727-733.
[6] J. E. Goff, M.J. Carre´, Soccer ball lift coefficients via trajectory analysis, Eur. J. Phys. 31 (2010) 775-784.
[7] S. Barber, S.B. Chin M.J. Carré, Sports ball aerodynamics: A numerical study of the erratic motion of soccer balls, Computers & Fluids 38(6) (2009)1091-1100.
[8] F. Alam, G. Zimmer, S. Watkins, Mean and time-varying flow measurements on the surface of a family of idealized road vehicles, Experimental Thermal and Fluid Sciences. 27 (2003) 639-654.
[9] E. Achenbach, Experiments on the flow past spheres at very high Reynolds numbers, Journal of Fluid Mechanics. 54 (1972) 565–575.
[10] S. Barber, S.B. Chin M.J.Carré, Sports ball aerodynamics: A numerical study of the erratic motion of soccer balls, Computers & Fluids. 38(6) (2009) 1091-1100.
[11] L. Oggiano, L. Sætran, Aerodynamics of modern soccer balls, Procedia Engineering. 2(2) (2010) 2473-2479.

Available online at www.sciencedirect.com

ScienceDirect

Procedia Engineering 00 (2015) 000–000

Procedia Engineering

www.elsevier.com/locate/procedia

6th BSME International Conference on Thermal Engineering (ICTE 2014)

Numerical investigation on the delay of boundary layer separation by suction for NACA 4412

R. Azim[a]*, M. M. Hasan[a] and Mohammad Ali[b]

[a]*Department of Mechanical Engineering, Bangladesh University of Engineering & Technology (BUET),Dhaka-1000.*

[b] *Professor,Department of Mechanical Engineering, Bangladesh University of Engineering & Technology (BUET),Dhaka-1000.*

Abstract

Transition flow over airfoils at the higher angle of attack shows a lot of unsteady phenomena such as local separation regions, boundary layer transition, turbulence and shock boundary layer interaction. These phenomena are associated with high energy loss and adversely effects the aerodynamic loads in the form of lift loss and drag increase. Controlling the flow through separation delay by suction at different slots, by flaps, by introducing bumps and sophisticated high lifting devices can mitigate the aerodynamic losses. This paper focuses on the delay of boundary layer separation of 2D NACA 4412 by suction using CFD analysis. Picking out the right suction position augments the aerodynamic performance. So a slot with a width of 2% of the chord length is placed at five different locations starting from 48% to 70% of the chord length. The main part of the paper is related to the selection of a suction position and outcome of different suction pressures at a definite slot. Suction with the lower pressure at a definite position moves the separation of boundary layer in the vicinity of trailing edge of the airfoil most. By suing suction at suction pressure 65kPa on 68% of the chord length of the airfoil with a constant angle 2^0 with the upper surface of the airfoil, AOA=13^0 and M=0.6, it is possible to move the transition to turbulent flow about 91% of the chord length of the airfoil near the trailing edge where it is found at 43% of the chord length of the airfoil without suction. So the laminar region is extended and the lift increases. Along with this, at low angle of attack, the lift to drag ratio after suction increases about 2.24 times compared to that of without suction.

© 2015 The Authors. Published by Elsevier Ltd.

Peer-review under responsibility of organizing committee of the 6th BSME International Conference on Thermal Engineering (ICTE 2014).

Keywords: Flow control ; Laminar flow ; Turbulent flow ; Lift and drag force ; Boundary layer separation ; Pressure co-efficient

Nomenclature and abbreviation

M	Mach number
AOA	Angle of attack

* Corresponding author. Tel.: +8801911560549

E-mail address: riasatme08@gmail.com

1877-7058 © 2015 The Authors. Published by Elsevier Ltd.

Peer-review under responsibility of organizing committee of the 6th BSME International Conference on Thermal Engineering (ICTE 2014).

NACA	National Advisory Committee for Aeronautics

1. Introduction

The turbulent flow separation around the trailing edge (TE) of an airfoil affects the aerodynamic performances (like lift reduction, drag enhancement) very severely. At the higher angle of attack, the effect of adverse pressure gradient enhances the formation of separation wakes around trailing edge of the airfoil. The application of suction at proper position greatly subjugates the stream wise momentum loss in the wake. For the past years, considerable effort had been devoted to the investigation of the application of suction applied either through open slit or porous wall strip for the purpose of reduction of the skin friction drag or for the control of the boundary layers. Braslow [1] illustrated the history of suction type laminar flow control. Seifert et al. [2] investigated unsteady suction and blowing on a symmetric airfoil to increase post-stall lift. Two different means of suction had been investigated in the past: discrete suction through slots and distributed suction. Boermans [3] had shown that discrete suction allowed an abrupt pressure increase at the location of the slot. Eppler [4] found that the design case of an airfoil with distributed suction specifies together with the suction compartments and the suction pressure, the porosity of the surface. Oyewola et al. [5] studied that the effects of localized double suction applied through a pair of porous wall strips on a turbulent boundary layer had been quantified through the measurements of mean velocity and Reynolds stresses. Richards et al. [6] had shown that, it was impossible to maintain laminar flow aft of the suction slot at high Reynolds numbers because of the dynamic instability of the laminar layer over the concave surface. So the porosity of the surface of airfoil and geometry of the suction compartments are determined by the designed case. That's why, it is considered that many off-design cases like surface porosity and suction compartment geometry are fixed and the pressure in the suction slot is the only variable for numerical investigation over an airfoil like NACA 4412.

2. Numerical procedures

Navier–Stokes equations arise from applying Newton's second law to fluid motion, together with the assumption that the fluid stress is the sum of a diffusing viscous term (proportional to the gradient of velocity) and a pressure term - hence describing the viscous flow. In an inertial frame of reference, the general form of the equation is:

$$\rho\left(\frac{\partial v}{\partial t} + v.\nabla v\right) = -\nabla p + \nabla.T + f$$

Where,$\boldsymbol{v}$ is the flow velocity, ρ is the fluid density, p is the pressure, T is the stress tensor, f represents body forces (per unit volume) acting on the fluid and ∇ is the Del operator.

Numerical flow simulation is performed by solving Navier-Stokes equations, which are formulation of mass, momentum and energy conservation laws.

The Spalart Allmaras [7] turbulence model solved a modelled transport equation for kinematic eddy viscosity without calculating the length scale related to the shear layer thickness. The variable transported in the Spalart Allmaras model is $\tilde{\nu}$ which is assimilated, in the regions which are not affected by strong viscous effects such as the near wall region, to the turbulent kinematic viscosity. This equation has four versions, the simplest one is only applicable to free shear flows and the most complicated, which is written below, can treat turbulent flow past a body with laminar regions.

$$\frac{\partial}{\partial t}(\rho\tilde{\nu}) + \frac{\partial}{\partial x_i}(\rho\tilde{\nu}\, u_i) = G_v + \frac{1}{\sigma_{\tilde{\nu}}}\left[\frac{\partial}{\partial x}\left\{(\mu + \rho\tilde{\nu})\frac{\partial\tilde{\nu}}{\partial x}\right\} + C\,\rho\left(\frac{\partial\tilde{\nu}}{\partial x_i}\right)^2\right] - Y_v + S_{\tilde{\nu}}$$

This transport equation brings together the turbulent viscosity production term,G_v and the destruction term, Y_v.The physics behind the destruction of turbulence occurs in the near wall region, where viscous damping and wall blocking effects are dominants. No heat generation or transfer is considered. The other terms or factors are constants calibrated for each physical effect which needs to be modelled. This equation allows to determinate $\tilde{\boldsymbol{\nu}}$ for the computation of the turbulent viscosity, μ_t from:

$$\mu_{t=}\,\rho\tilde{\nu}\, f_{v1}$$

The cell centred finite volume method (FVM) is used to obtain conservative approximations of the governing equations on the locally refined rectangular mesh. The governing equations are integrated over a control volume which is a grid cell and then approximated with the cell centred values of the basic variables. The integral conservation laws may be represented in the form of the cell volume and surface integral equation:

$$\frac{\partial}{\partial x}\int U dv + \oint \bar{r}.ds = \int Q\, dv$$

This is replaced by

$$\frac{\partial}{\partial t(Uv)} + \sum_{Cell\ faces} F.S = Qv$$

3. Result and discussion

3.1 Validation

Computations are performed for a NACA 4412 airfoil to test the grid independency. So a finer mesh, made of 89800 quadrilateral cells, 90598 numbers of nodes is compared with a mesh of 14670 quadrilateral cells and 14981 numbers of nodes with the same input of AOA=12^0 and M=0.6. The lift co-efficient found for the finer mesh is 1.36 and varies with that of the other mesh by 0.75% which is concurrent to the independency test.

For the validation of the data of without suction, the pressure coefficient versus position curve is studied. The result obtained in simulation is compared with the theoretical data of Pinkerton [8] and the experimental data of Heffley and Trueren [9] for angle of attack = 10^0. The maximum variation of the simulated data is found at about 40% of the chord length of the airfoil by 4.2% with that of the experimental result.

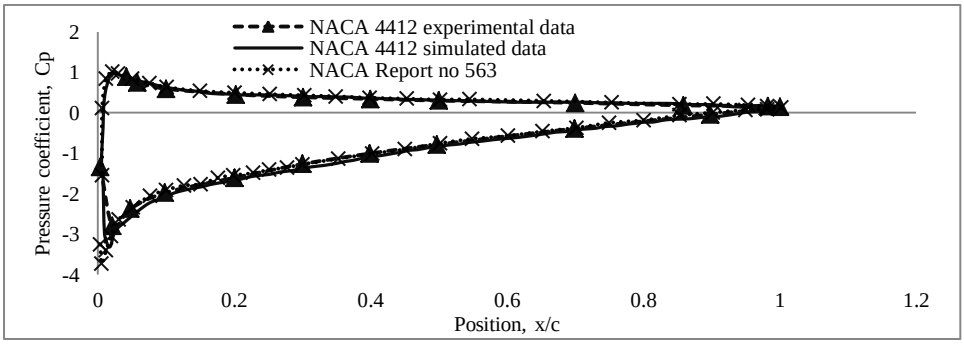

Fig. 1. Data validation for AOA=10^0 of NACA 4412 airfoil.

In case of the suction, the exact experimental data is not available. So the simulated data is compared with the most nearest data available. Goodarzi et al. [10] had worked with NACA 0012 with slots located at different position with different suction rations. So the findings of the simulation are compared with their research but a complete match isn't found with the observed conditions. In that case, slot situated at 80% of the chord from the leading edge was not capable of delaying or reducing the separation of boundary layer. On the contrary, slots situated at 0.68c not only delayed the separation but also reduced the amount of wakes significantly.

a)

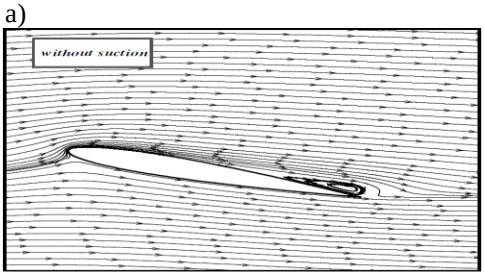

b)

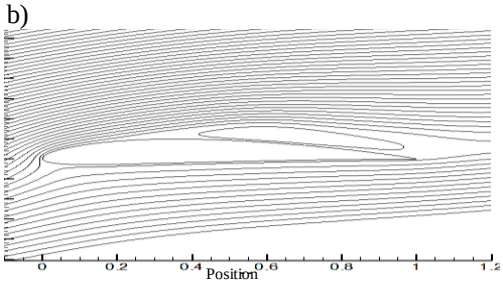

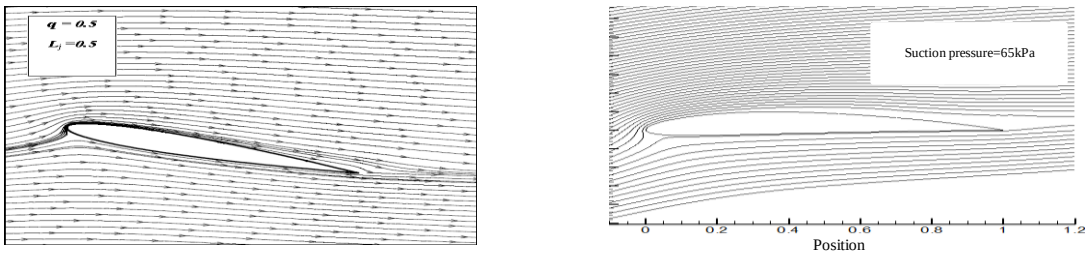

Fig.2. Research result of Goodarzi et al. vs. the simulated result.
a) and b) without suction; c) and d) with suction.

3.2 Slot selection

Suction in the proper position increases the aerodynamic performances. But choosing the best position depends on various parameters which makes the decision complex. Mach number, angle of attack (AOA), suction pressure etc. affect the position of suction. To lessen the enormous complexities, the aerodynamic performance is measured at various position on the upper surface of the airfoil at a suction pressure 75kPa keeping Mach number and AOA constant at 0.6 and 12^0 respectively.

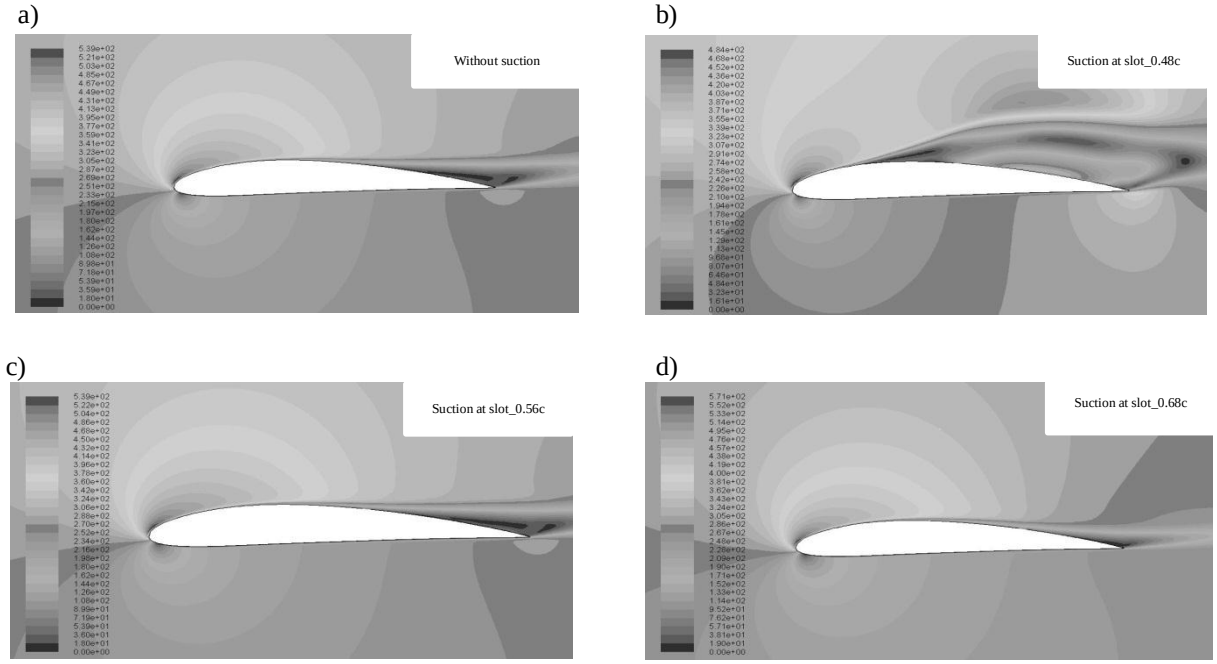

Fig. 3. Velocity contour for AOA=12^0 (a) without suction; (b) with suction at slot_0.48c;
(c) with suction at slot_0.56c and (d) with suction at slot_0.68c of the airfoil at constant suction pressure 75kPa.

For without suction, the trailing edge separation is found around 0.7c from the leading edge of the airfoil. But suction close to the trailing edge separation, i.e. at slot_0.68c, moves the separation more in the vicinity of the trailing edge, about 0.88c from the leading edge of the airfoil. On the contrary, the earlier suction such as slot_0.56c and slot_0.48c decreases the performance drastically shown in Fig. 3. (b and c). Eventually suction at slot_0.48c decreases the lift, increases the turbulence and gives fully the adverse effect. This suggests that moving the slot downstream will produce a greater separation delay. Due to the increase in turbulence, the skin friction contributes the drag coefficient to increase about 6 times than that of without suction. The lift also decreases slightly. So lift to drag ratio falls off drastically. But suction at slot_0.68c decreases the drag coefficient from 0.043 to 0.03 which

results 35.6% increase in lift to drag ratio from that of without suction. So eventually, for better aerodynamic performance, suction is done at slot_0.68c.

3.3 Effect of suction pressures on lift to drag ratio at constant M=0.6

Lift co-efficient for M=0.6 is more or less straight forward for lower AOAs. For higher AOAs, local pressure near the suction region is so closed that suction pressure of 80kPa has no substantial effect on the flow field. For this reason, suction is not as effective for higher suction pressure like 80kPa as in the case of above AOA=5^0. Suction with sufficiently low pressure like 70kPa, 65kPa drops-off this phenomenon and suction is still effective for higher AOAs. Hence, lines with lower suction pressure remain above for higher AOAs than that of without suction shown in Fig. 4. (a).

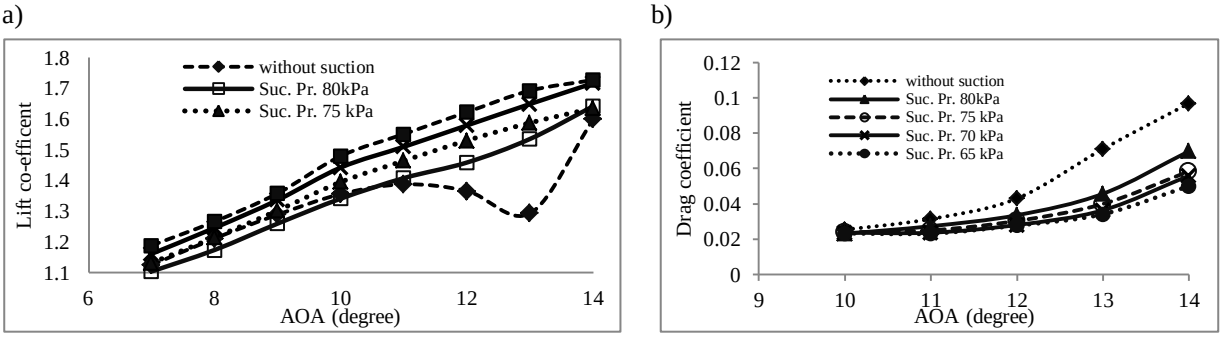

Fig. 4. (a) Lift co-efficient vs. AOA; (b) Drag co-efficient vs. AOA.

For lower AOAs, suction is effective for drag reduction. On the contrary, it is not so in the moderate AOAs. Apart from that, suction greatly subjugates drag coefficient in higher angle of attack. For higher angle of attack, trailing edge turbulence separation is delayed with suction. That is why; suction is effective for higher AOAs, seen in Fig. 4.(b).

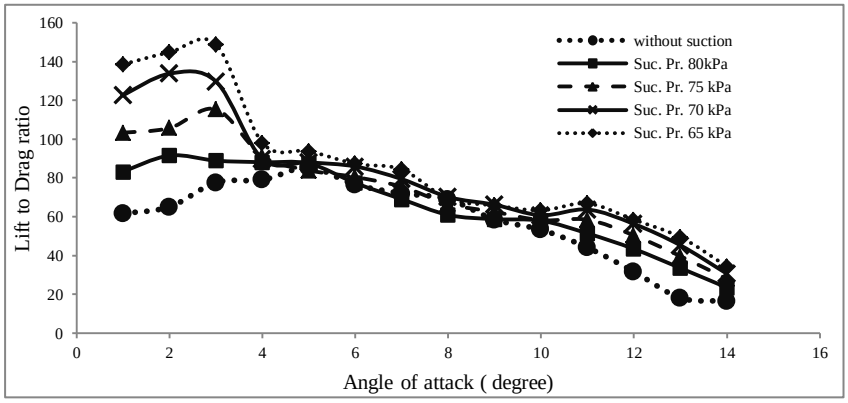

Fig. 5. Change of lift to drag ratio with AOA for different suction pressures.

In lift to drag ratio curve from Fig 5, lowering the suction pressure augments the lift to drag ratio with a clear view for lower AOAs. For higher AOAs, stalling is prevented with lowering suction pressure. Concluding these two phenomena, suction is welcome both for the lower AOA application like steady level flight and for the higher AOA application like take-off operation.

3.4 Trailing edge separation for different suction pressure

Separation position moves in the vicinity of the trailing edge with the decrease of suction pressure. Initially the gradual decrease in the suction pressure moves the separation position towards the trailing edge in a great extent but later on; decrease in pressure moves the separation position slightly towards the trailing edge. So for a definite AOA=12^0, separation position moves from 0.76c to 0.91c of the airfoil for change of suction pressure from 80kPa to 70kPa and later on for the suction pressure 65kPa, it moves to 0.96c of the airfoil. Changes in separation position from leading edge with the decrease in suction pressure shown in Fig. 6.

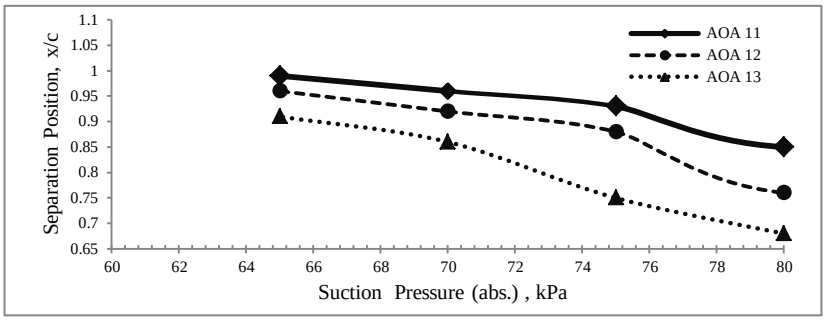

Fig. 6. Change in trailing edge separation position with different suction pressures.

4. Conclusion

The numerical investigation on the aerodynamic performance for the delay of boundary layer separation by suction in NACA 4412 airfoil surface leads to the certain concluding remarks. Slot in the vicinity of the trailing edge produces a greater separation delay. For AOA=12^0 and M=0.6, suction at slot_0.68c of the airfoil with a suction pressure 65kPa moves the formation of separation bubbles from 0.7c to 0.96c of the airfoil. Though the effect of turbulent separation is not dominant in the lower AOAs, suction in that case enhances the lift coefficient significantly and reduces the drag slightly. As a result lift to drag ratio during suction is approximately 2.24 times higher than that of without suction. For the higher AOAs, suction increases the aerodynamic performances and delays stalling. Suction with lower pressure produces the delay of the trailing edge separation far downstream than the higher pressure. So for a constant AOA=12^0 and M=0.6, suction with 65kPa at slot_0.68c moves the separation position about 0.96c of the airfoil but it is found at 0.76c of the airfoil when suction is done at 80kPa at the same slot. Along with this, suction with 65kPa makes lift to drag ratio 35% higher than that of suction at 80kPa.

References

[1] A. L. Braslow, A history of suction-type laminar-flow control with emphasis on flight Research, Monographs in Aerospace History #13, NASA History Division Office of Policy and Plans, NASA Headquarters Washington, DC 205469,1999.

[2] A. Seifert, T. Bachar, D. Koss, M. Shepshelovich, and I. Wygnanski, Oscillatory blowing: A tool to delay boundary-layer separation, AIAA Journal, 31(11), 1993.

[3] L.M.M. Boermans, Glide ratio 1:80, A solar challenge?, Paper at XXV OSTIV Congress St. Auban, France, 1997.

[4] R. Eppler, Airfoils with boundary layer suction, design and off-design cases, Aerosp. Sci. Technol. 3, 1999, pp. 403–415

[5] O. Oyewola, L. Djenidi, R.A. Antonia, Influence of localised double suction on a turbulent boundary layer, Journal of Fluids and Structures 23, 2007, pp. 787 – 798.

[6] E. J. Richards, W. S. Walker and C. R Taylor, Wind-tunnel tests on a 30 per cent. suction wing, R. &M. no. 2149 (8864), A.R.C. Technical Report, 1945.

[7] P.R. Spalart and S.R. Allamaras, A one equation turbulence model for aerodynamic flows, AIAA Paper 92-0439, 1992

[8] R. M. Pinkerton, Calculated and measured pressure distribution over the mid span section of the NACA 4412 airfoil, NACA report no. 563, 1937.

[9] D. Heffley and V. Treuren, Aerodynamic characteristics of a NACA 4412 airfoil, Scholars' Day, Baylor University, January, 2007.

[10] M. Goodarzi, R. Fereidouni, and M. Rahimi, Investigation of flow control over a NACA 0012 airfoil by suction effect on aerodynamic characteristics, Canadian Journal on Mechanical Sciences & Engineering Vol. 3 No. 3, June 2012.

Passive Control of Shock Oscillation around a Biconvex Circular Arc Airfoil in a Channel

*Md. Abdul Hamid and A.B.M. Toufique Hasan**

Department of Mechanical Engineering, Bangladesh University of Engineering & Technology (BUET), Dhaka-1000, Bangladesh

* toufiquehasan@me.buet.ac.bd

Abstract

A strong normal shock wave, generated on an airfoil, is responsible not only for limiting the aerodynamic performance but also for shock induced boundary layer separation. This shock induced boundary layer separation results aerodynamics instabilities (buffet), high cycle fatigue failure (HCF), nonsynchronous vibration (NSV), flutter and so on. In the present study, a numerical computation has been performed to control the unsteady shock oscillation over a 12% biconvex circular arc airfoil in a two dimensional channel. Reynolds averaged Navier-Stokes equations with k-ω shear stress transport (SST) two equation turbulence model has been applied for computational analysis. To control the shock oscillation over a biconvex circular arc airfoil (referred as base airfoil), the geometry of the base airfoil has been modified by incorporating a cavity with two openings on both upper and lower surface of the airfoil. The cavity has been incorporated in such a manner that the mean position (along chord length) of the cavity is placed where the RMS of static pressure fluctuation on airfoil surface (for base airfoil) is maximum. The length and depth of the cavities are kept 10% and 2% of the chord length respectively to avoid the structural failure. The behavior of the shock wave oscillation has been studied for a particular pressure ratio (defined as the ratio of back pressure to inlet total pressure) of 0.69. The present study investigates the shock wave characteristics over (a) airfoil with no cavity (base airfoil) (b) airfoil with cavity with 40% opening (40% of cavity length is open) and (c) airfoil with cavity with 60 % opening. The results show, incorporating cavities on airfoil surfaces not only affect the flow field but also change its behavior in a great extent. For pressure ratio 0.69, the flow field becomes steady for airfoil with cavities (both 40% and 60%) while for base airfoil the flow field was unsteady. The results also show that incorporating a cavity on airfoil surfaces changes the type of shock wave from normal to λ shock wave. For base airfoil the maximum shock mach number (M_s) varies ranging from 1.24 to 1.3 while for airfoil with cavities with 40% and 60% opening, M_s become 1.24 and 1.23 respectively.

Computational Investigation of Aerodynamic Hysteresis for Transonic Flow over a Supercritical Airfoil

M. Rizwanur Rahman, A.B.M. Toufique Hasan, and M. Itmam Labib*

Department of Mechanical Engineering, Bangladesh University of Engineering and Technology (BUET), Dhaka 1000, Bangladesh

* toufiquehasan@me.buet.ac.bd

Abstract:

This paper numerically investigates the aerodynamic hysteresis for transonic flow over super critical airfoil RAE-2822 of a chord length of 0.61m. In the present study, Reynolds averaged Navier-Stokes equations (RANS) with Spalart-Allmaras turbulence model has been applied. The free stream transonic Mach number is kept as 0.729 and the angle of attack was increased from -5 degree to + 18 degree and then again decreased to -5 degree. The computations are carried out until fully developed flow is obtained and the fully developed solution obtained at a specific angle of attack is used as the initial condition for the computations of the next angle of attack. After successive computations, hysteresis loop is observed in the range of 7 degree to 11 degree. For the same angle of attack in the loop, the ascending branch exhibits higher lift and drag coefficients but lower unsteadiness while the descending brunch shows lower coefficients of lift and drag but higher unsteadiness and flow separation with associated strong vortex structure in the wake. The incoming stream is much attached in the ascending branch compared to that of the descending branch. The hysteresis is closely related to the laminar boundary layer separation and transitions on airfoil. The memory of the flow is responsible for this hysteresis.

.

Available online at www.sciencedirect.com

SciVerse ScienceDirect

Procedia Engineering00 (2015) 000–000

Procedia Engineering

www.elsevier.com/locate/procedia

6th BSME International Conference on Thermal Engineering (ICTE 2014)

Andrei Kozlov, Harun Chowdhury*, Israt Mustary and Bavin Loganathan and Firoz Alam

School of Aerospace, Mechanical and Manufacturing Engineering, RMIT University, Melbourne, 3083, Australia

Abstract

This paper investigates the aerodynamic behavior of a boxfish using both experimental and computational methods. A scaled up model boxfish was manufactured and tested in RMIT Industrial Wind Tunnel under a range of Reynolds numbers and yaw angles. The drag, lift and side forces and their corresponding moments were measured simultaneously. A CAD model of the boxfish was used in CFX FLUENT Computational Fluid Dynamics (CFD) modeling. The CFD modeling data were validated using the experimental findings. The results indicate that the drag coefficient of a boxfish is around 0.10 which is significantly lower than current drag coefficient of a passenger car. Hence, a boxfish shape can be adapted for achieving low drag and energy efficient motor vehicle design.

© 2015 The Authors. Published by Elsevier Ltd.
Peer-review under responsibility of organizing committee of the 6th BSME International Conference on Thermal Engineering (ICTE 2014).

Keywords: Passenger car; aerodynamic drag; box fish; wind tunnel; yaw angle; CFD.

1. Introduction

The concept of Biomimicry refers to the study and observation of how nature has been dealing with problems it has faced over at least 600 million years and applying it to human problems [1-2]. The concept itself is relatively new and only recent problems humanity has been facing, such as global warming, has been inspiring vehicle designers and aerodynamicists to explore a new ways of aerodynamic drag reduction. Due to only a recent emergence of biomimicry, there is no real procedure which defines how the process of biomimicry should be applied

* Corresponding author. Tel.: +61 3 99256103; fax: +61 3 99256108.
E-mail address: harun.chowdhury@rmit.edu.au

1877-7058 © 2015 The Authors. Published by Elsevier Ltd.
Peer-review under responsibility of organizing committee of the 6th BSME International Conference on Thermal Engineering (ICTE 2014).

to vehicle aerodynamic problems. The following steps have been thought out to allow for an initial step of implementation of biologically inspired design process into vehicle aerodynamics.

According to European Regulations, the CO_2 emission from a new vehicle in 2012 cannot be exceeded by 120 grams per kilometer and in 2020 this figure should be limited to 95 grams per kilometer [3]. Additionally, stiff market competition and rising fuel price force vehicle manufacturers to develop fuel efficient vehicles to be competitive and economically viable. One way to develop fuel efficient vehicles is the reduction of aerodynamic drag as it accounts for around 80% of the total drag at vehicle cruising speeds over 80 km/h [4]. The reduced drag will not only lower the fuel consumption but also the CO_2 emissions. The major drag reductions have been achieved by optimizing vehicle exterior body shapes over four decades. Further reduction can affect the vehicle styling – an important factor for customer perception (aesthetics) and marketing. The aerodynamic efficiency is more important for electric road vehicles due to the need of extension of operational range. Until recently road vehicle designs have been designed purely based on visual appreciation. Nature has been dealing with such problems for at least 600 million years and very often there is an optimized solution to a problem it has faced [1]. It is therefore evident that each evolution stage should be more efficient than the previous. Therefore, it should be beneficial for designers and aerodynamicist to choose nature as a mentor, and observe how previously nature has dealt with a problem, such as efficient propulsion through a medium.

The traditional box shape passenger cars in 1920s started to become more streamlined in 1960-70s as aerodynamics became a dominant factor to reduce the fuel consumption especially during the 1973-74 oil embargo by OPEC. The aerodynamic efficiency indicator (drag coefficient) started to fall from around 0.60 for a typical passenger car in 1960s to 0.40 in late 1970s and 0.28 in 2012. Further drag reduction in passenger cars is hard to achieve using already streamlined body shapes. Slight reduction in drag coefficient is still possible if smooth under body, smart wheel, reduced wheel wells and convoy driving (platooning) are used. However, the smooth under body, wheels and wheel arches deteriorate vehicle cooling performance. Therefore, an alternative body shape with lower drag coefficient is paramount. Despite having unpleasant appearance, the boxfish is considered to have lower aerodynamic resistance than dolphins and penguins. Thanks to its large cross section and structural rigidity, the boxfish is more suited to mimic in automobile body shapes. Some car manufacturers including Daimler-Chrysler are attempting to replicate the boxfish shape into their car designs. However, scant information is currently available in the public domain on boxfish aerodynamics. Therefore, the main objective of this study is to investigate the aerodynamic behavior of a boxfish using both experimental and computational methods.

Nomenclature

F_D	aerodynamic drag (N)
C_D	aerodynamic drag coefficient
Re	Reynolds number
V	wind velocity (m/s)
μ	absolute dynamic viscosity of wind (Pa)
ρ	air density (kg/m^3)
A	projected frontal area of boxfish (m^2)

2. Methodology

2.1. Selection of a model

One problem with the integration of biomimicry with vehicle aerodynamics is the compatibility of a suitable model, which can be used and replicated. Very often the process of reduction in aerodynamic/hydrodynamic drag involves the reduction of frontal area which is encountered by the flow. This is very commonly seen in fish, as they tend to generally be long and slim as seen in a presentation by Choi [5], which reduces the pressure drag. They also have unique skin surfaces to reduce the associated skin friction. Such geometries are however not of much use for mimicking in vehicle aerodynamics. However, this does not apply to all species. In fact, many species in the

Ostraciidae fish family have very unique body geometries. Many of these fish from Ostraciidae are optimized for benefits other than hydrodynamic drag and are not suited to be used as a model. One example is the Horn-Nosed boxfish, captured by Randall [6]. Although it belongs to the same family, its extra "horn" like front is not desired in vehicle design. However, the yellow boxfish has a very simple box geometry without any additional geometric features which is desired for vehicle replication. Therefore, a yellow boxfish shape has been selected to study its aerodynamic behavior especially drag using both computational fluid dynamics (CFD) modeling and wind tunnel experimental study.

2.2. CFD modeling and wind tunnel testing

Modern CFD modeling techniques together with increasing computational capabilities are becoming much more of a viable tool to model various shapes including road vehicles. It also offers an alternative tool to costly wind tunnel experimentation. However, the wind tunnel data is still required to validate the CFD modeling findings. For the experimental study, the RMIT Industrial Wind Tunnel was used. It is a closed return circuit with a rectangular test section of 6 m^2 (3 m wide, 2 m high and 9 m long). The maximum speed of the wind in the test section is approximately 145 km/h. More details about the tunnel can be found in Alam et al. [7]. A physical model of simplified boxfish was designed and manufactured. The model was made of Styrofoam. A device was developed to hold the model with a 6-component force sensor (made by JR3 Inc., USA) to measure all 3 forces (drag, side and lift/down forces) and 3 moments (yaw, roll and pitch) simultaneously. The aerodynamic drag forces were measured over a range of wind speeds (20 to 100 km/h with an increment of 10 km/h). The drag forces were converted to non dimensional parameter drag coefficient (C_D). The aerodynamic drag coefficient (C_D) and the Reynolds number (Re) are defined as:

$$C_D = \frac{D}{\frac{1}{2}\rho V^2 A} \tag{1}$$

$$Re = \frac{\rho V d}{\mu} \tag{2}$$

The lift and side forces and their coefficients were not determined and presented in this paper. Only drag data is presented here.

The CFX (version 14.5) was used to model the airflow around the model. A CAD model was developed using CATIA. Two turbulence schemes (standard k-ω and k-ε) were used to model the flow around the CAD model. Preparation of the simplified boxfish model for CFD modeling was accomplished through the process of mimicry. A specific yellow boxfish was used as a baseline for the simplified model as shown in Fig 1(a). The simplification involved the idealization of the boxfish model from the real yellow boxfish with addition of idealization in order to create the model. The idealization of the model was most noticeable at the front and rear where the mouth and tail regions of the fish are located. These were idealized and incorporated to the main body which was replicated as accurately as was possible. Due to the file conversion process, careful attention was devoted to achieving a CFD model which was as close to CAD model as possible, which was achieved through a selected conversion settings. Once the model was incorporated into the idealized wind tunnel test section in CFD domain, the wind tunnel atmosphere was modeled by incorporating the stationary simplified boxfish model. For the Reynolds number sensitivity tests, the wind tunnel environment was halved as seen in Fig. 4 due to symmetry, which allowed much faster simulation times to be achieved, as well as allow further local mesh refinement in close proximity to the simplified boxfish model. For comparison, the tests were also replicated with full size wind tunnel geometry. The wind tunnel model and setup is shown in Fig. 1(b).

The methodology of all computational work utilizes a hybrid mesh consisting of unstructured triangular and tetrahedral mesh, throughout the entire volume of the wind tunnel environment. An additional layer in the region of surface of the boxfish model with finer surface mesh is added in order to more correctly predict the flow separation

and flow phenomena in close proximity to the boxfish model. Furthermore, a box of influence is added to the wind tunnel environment, in order to effectively distribute finer mesh to the region where flow phenomena must be more accurately evaluated, the meshing setup for the Reynolds number sensitivity tests can be seen in Fig. 2. A similar approach is used for the yaw test. The box of influence has a much greater concentration of mesh, thereby greatly reducing any unnecessary flow evaluation and simulation time in regions further away from the sides of the boxfish model.

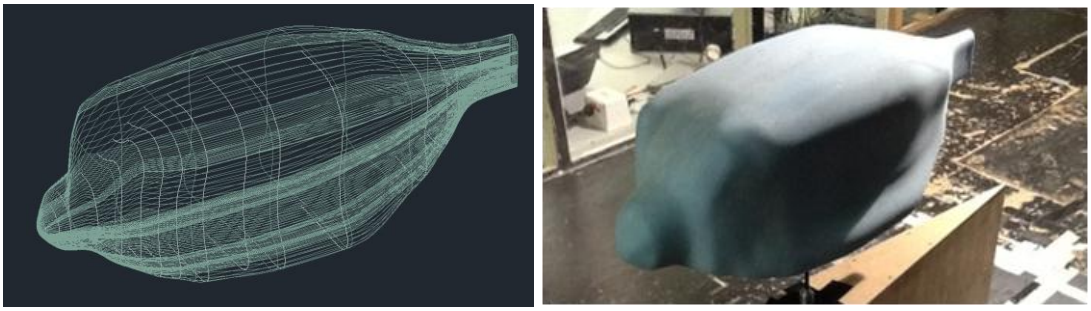

Fig. 1. (a) computational model; (b) wind tunnel model.

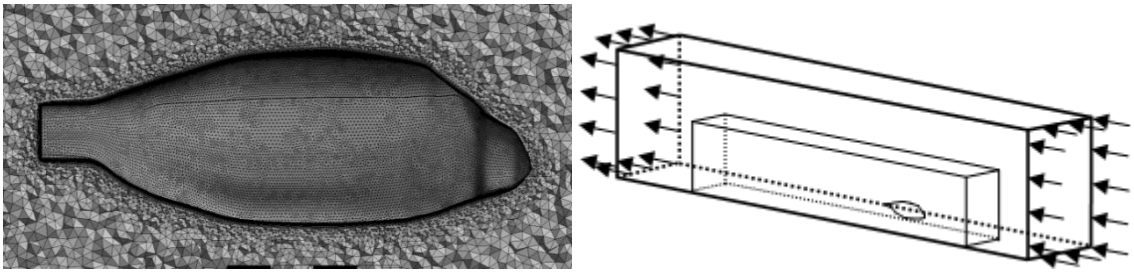

Fig. 2. (a) generated mesh for boxfish model; (b) schematic setup of half model tests.

In order to satisfy all requirements of both turbulence models, different meshing approaches were made for both the inflation layer and box of influence, in the case of *k-ω*, the mesh was reduced in order to minimize the mesh size increase as much as possible, due to the small first layer height required to achieve the desired y+ for the turbulence model. The settings used for both turbulence models and respective meshes are summarized in Table 1, and the setup in Fig. 2(b).

Table 1. Meshing summary for non yaw tests.

	k-ε	*k-ω*
Surface element size	25 (mm)	0.025
Inflation setting	First aspect ratio (scalable wall function)	First layer thickness (automatic wall function)
Maximum number of layer	5	50 (30)
First aspect ratio	5	-
First layer height	-	0.004 (mm)
Y+ (typical)	29 - 65	0.012 – 1.6

Two tests for *k-ω* were completed; one is classified as a stable and the other as non-stable. Due to the known instability of the turbulence model/common convergence issues, the non-stable case is that which the residuals are isolating between a value of 10^{-3} and a stable case in which all residuals isolate in close proximity to 10^{-5} however do not meet the convergence target of 10^{-5} which was set for both turbulence model cases. However, in all tests, the drag convergence was prioritized before residual convergence. The fluid and boundary properties for both CFD modeling are shown in Table 2.

Table 2. Boundary conditions and fluid properties.

Boundary properties	
Inlet wind speed	20, 40, 60, 80 and 100 km/h
Outlet wind speed	Average static pressure = 0
Wind tunnel walls	All symmetry
Model wall	No slip wall
Fluid property	Air at 25 °C (isothermal)

3. Results and discussion

Fig. 3(a) shows the drag coefficient convergence characteristics of the simplified boxfish model for the standard k-ε turbulence model. All tests were conducted for inflow velocities of 20−100 km/h which equate to the corresponding Reynolds number as seen in Fig. 3. From Fig. 3(a), a clear convergence was observed as the mesh was refined to 8 million elements, it was important to achieve this convergence to increase the confidence of obtaining a correct result based on the selected turbulence model. Like satisfying y+ requirements for the turbulence model used, it was important to achieve this convergence to the maximum available computational mesh quantity, which was around 9 million elements of unstructured mesh. Fig. 3(b) shows the variation between the described stable case (50 layers) and non-stable case (30 layers) as well as *k-ε* and currently available wind tunnel data. From Fig. 3(b), the varying difference of prediction between both turbulence models was noted. At lower *Re* numbers, *k-ε* was found to under predict where as *k-ω* over predicted C_D, however there are some doubts of the accuracy of the wind tunnel used for lower *Re* numbers. For most cases *k-ω* predicted the results slightly better than *k-ε*, however due to its large computational time, it was less efficient when comparing the accuracy/simulation time of the two turbulence models used. It was found that the wind tunnel data also more closely match the less stable *k-ω* case, which had not fully converged to the 10-5 residual target, during which the C_D had also been slightly more unstable. Due to the high likelihood of wind tunnel inconsistencies and equipment errors/limits, it could explain the higher drag readings for most *Re* number cases.

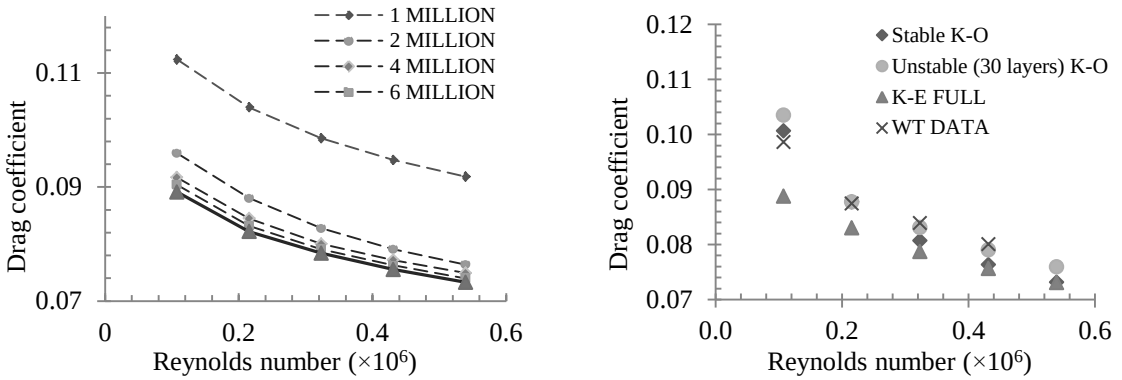

Fig. 3. (a) drag coefficient convergence characteristics; (b) drag coefficient variation with Reynolds number.

Apart from numerical data, the post analysis results were further studied to study the flow features around the simplified model. The flow features around the model are shown in Fig. 4 and Fig. 5. Fig. 4 shows the two main methods the simplified boxfish model achieves low drag characteristics. The front view indicates a transition of the inflow into four main regions; the unique shape allows transition into the back view with very little flow separation, which is mainly observed at the idealized mouth region, which was also found to be a region of improvement which may lead to lower C_D. The rear view indicates three vortices forming per side, which are generally not desirable, however, are shape specific. The main drag reduction from the back view is achieved through the diffusion process from all sides, which effectively contribute to the pressure recovery of the flow and reduce the C_D. Fig. 5(a) shows the flow characteristics of the airflow around the simplified model. Due to the sharp rear diffusion angle, flow

separation is inevitable, even for a Re number of 0.1×10^6. Fig. 5(b) shows the static pressure characteristics at a *Re* number of 0.1×10^6, similar to that of Fig. 5(a). It can be seen that regions of relatively high pressure exist near the idealized region as well as a diffusion region during which pressure recovery is occurring located at the rear of the simplified model.

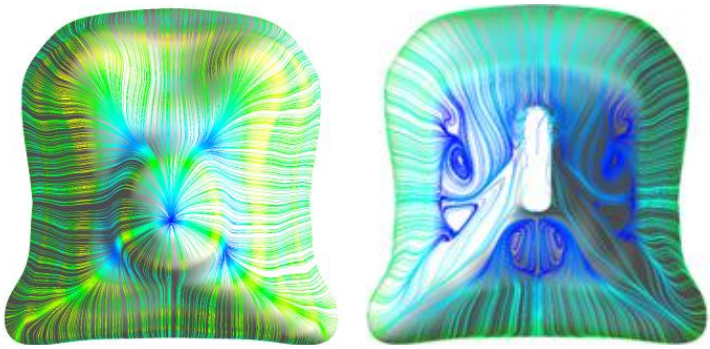

Fig. 4. surface streamline characteristics (k-ε): (a) front view; (b) rear view.

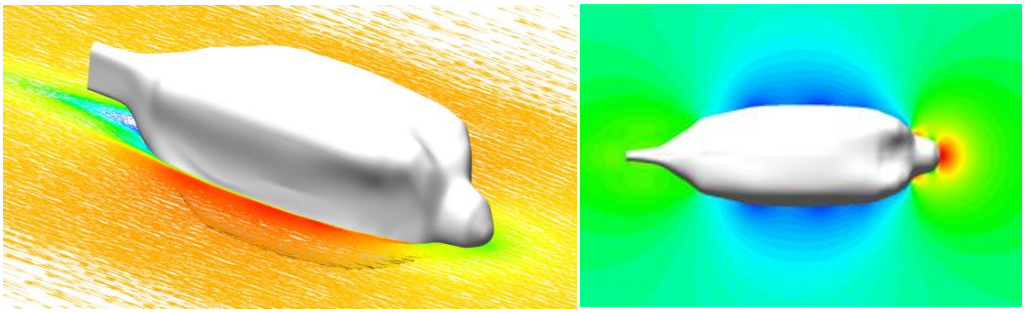

Fig. 5. (a) velocity vector for simplified model; (b) static pressure characteristics of simplified model.

4. Conclusions

The drag characteristics of a simplified boxfish model were studied and it was found that a similar geometry to that of a boxfish has very favourable drag characteristics for such a bluff geometry. CFD has allowed the study of flow characteristics of the simplified model to be studied, together with currently available wind tunnel data and mesh convergence studies, confidence in the CFD results had been established, despite slight variation between the two standards: k-ω and k-ε, an overall agreement at higher Reynolds numbers was achieved. The simplified model displayed a favorable drag coefficient of 0.073 at a Reynolds numbers equivalent to 100 km/h inflow velocity. Boxfish geometry was found to be a very efficient at minimising the disturbance of flow through the tested medium.

References

[1] S. Peter, J.H.K.S. Fiske, Lean, Light and Quiet: Advances in Automotive Energy Efficiency through Biomimetic Design. SAE International, SAE Technical Paper. (2008-21-0028).
[2] M.P. Zari, Biomimetic approaches to architectural design for increased sustainability, School of architecture, Victoria University, NZ, 2007.
[3] European Automobile Industry Report2009/2010. ACEA: www.acea.be [accessed on 10 December 2011].
[4] W.H. Hucho, Aerodynamics of Road Vehicles, 4th ed., SAE International, USA, 1998.
[5] H. H. Choi, H. Park, W. Sagong, Biomimetic flow control based on morphological features of living creatures, Physics of Fluids, 24 (2012) 121302.
[6] J.E. Randal, Ostracion rhinorhynchos, Fishbase.org, [accessed on 10 December 2011]
[7] F. Alam, G. Zimmer, S. Watkins, Mean and time-varying flow measurements on the surface of a family of idealized road vehicles, Experimental Thermal and Fluid Sciences. 27 (2003) 639-654.

Stability of disturbance waves in developing shear flows: A review of adhoc methods

P. K. Sen, S. Hegde and A. R. Paul

Department of Applied Mechanics, Indian Institute of Technology,
New Delhi 110-016, India.

Abstract

This paper attempts to induce some formalism in the study of stability of developing shear flows, by use of so called `ad-hoc' methods wherein all terms upto and inclusive of a particular order are lumped together in the same equation. The classical example of stability of a developing shear flow is the stability problem of boundary-layer flow over a flat-plate including the non-parallel effects. Other examples are free shear flows; also, problems involving flow over alternate rigid and porous panels with suction, or suction from one plate and injection from the opposite plate. The quick method for stability analysis is to use the local Orr-Sommerfeld solution, using the quasi-parallel approximation. This is sometimes augmented by inclusion of some non-parallel terms, perhaps in an ad-hoc manner, and so called `improved solutions' are obtained. The present paper attempts to establish a formal framework for these methods so that these methods are no more termed `ad-hoc'.

Available online at www.sciencedirect.com

ScienceDirect

Procedia Engineering 00 (2015) 000–000

Procedia Engineering

www.elsevier.com/locate/procedia

6th BSME International Conference on Thermal Engineering (ICTE 2014)

Stability of flow past alternate rigid and compliant panels in Boundary layer flow and in channel flow

A. R. Paul[a], P. K. Sen[a] and S. Hegde[a]

[a]*Department of Applied Mechanics, IIT Delhi, New Delhi 110016, India.*

Abstract

Propagation of two-dimensional small amplitude Tollmien-Schlichting(TS) waves has been investigated over a rigid panel followed by a porous panel in the presence of cross-flow. In the present work two problems have been solved, viz., (i) boundary layer flow over alternate rigid-porous panels in which suction is applied through the porous panel; and (ii) flow past an alternate rigid porous channel in which cross flow is applied through the porous panel. Thus in case of the channel, there is injection through one wall and there is equal suction through the other wall.

Detailed two-dimensional analyses have been done for the disturbance waves using both the quasi-parallel (QP) approximation, and more accurately, using the non-parallel (NP) approach. The non-parallel approach has been carried out over the developing mean-flow region of the porous panel, following the rigid-porous junction.

Numerical solutions have been obtained by finite difference procedures. In some of the cases results have been validated with the available literature. Finally, the jumps in the amplitude of the disturbance waves across the rigid-porous junction were calculated using the theory of Sen et al. (JFM 2009).

The important outcome from this work is in optimizing the length of the porous panel, following the rigid-porous junction. It is seen that, as compared to the length required to approach the asymptotic mean flow state to within 99%, only a very short porous panel length is sufficient to stabilize the disturbances.

Hence, it is foreseen that alternate long rigid panels, with in-between short porous panels, could be a very effective way of stabilizing the disturbances, and thus delaying laminar to turbulent transition.

Keywords: Tollmien-Schlichting(TS); quasi-parallel; non-parallel; amplitude jump

1877-7058 © 2015 The Authors. Published by Elsevier Ltd.
Peer-review under responsibility of organizing committee of the 6th BSME International Conference on Thermal Engineering (ICTE 2014).

Available online at www.sciencedirect.com

ScienceDirect

Procedia Engineering 00 (2015) 000–000

Procedia Engineering

www.elsevier.com/locate/procedia

6th BSME International Conference on Thermal Engineering (ICTE 2014)

Stability of weak confined wake behind a cylinder in fully developed turbulent channel flow

T Vijaya Kumar[a], P.K. Sen[b]*, S.V Veeravalli[b] and Munendra Kumar[a]

[a]Delhi Technological University, Delhi 110042, India
[b]Indian Institute of Technology Delhi, New Delhi -110016, India

Abstract

The motivation for the study of instability of turbulent wake flow in a confined turbulent channel was multi-fold. First, the instability of confined wake flows has not been studied much. Second, confined wakes are found to retain their mean velocity profile for a considerable downstream distance. Third, wakes have two points of inflection, one each on either side of the centre line. The basic aim of the present study was to investigate the correlation between the turbulence in the wake region and the inflection points in the wake region using stability theory. The wake behind a cylinder of diameter d in a turbulent channel with half width h, is a weak confined wake when $d/h \approx 0.2$. Thus, $d/h = 0.2$ was chosen for the present work. Experimental results are obtained by introducing organized disturbances in the wake and tracking these downstream. Theoretical results were obtained by solving the Orr-Sommerfeld equation by numerical methods.

© 2015 The Authors. Published by Elsevier Ltd.
Peer-review under responsibility of organizing committee of the 6th BSME International Conference on Thermal Engineering (ICTE 2014).

Keywords: Stability theory; weak wake; inflection point; Karman vortices; turbulence tuner

1. Introduction

The basic task of hydro-dynamic stability theory is to explain all possible phases of transition from the laminar flow regime into the turbulent one in various dynamic systems of fluid mechanics. For near wall turbulence, the process of formation of lift-up and bursting of streaks has qualitative similarity to that of transition in a macroscopic perspective. This, and other examples like free shear flows, lead to interest in study of turbulence by asking the question: Are hydrodynamic instability mechanisms relevant in turbulent flows? In this context researchers have

* Corresponding author. Tel.: +91 9810846032
E-mail address: pksen@am.iitd.ac.in; pksen45@hotmail.com

1877-7058 © 2015 The Authors. Published by Elsevier Ltd.
Peer-review under responsibility of organizing committee of the 6th BSME International Conference on Thermal Engineering (ICTE 2014).

explored stability theory for studying some aspects of turbulence. Our present study focuses on a confined weak wake in fully developed turbulent channel flow.

The main difference between wakes and other flows, like wall bounded flows, and other free shear flows, is the presence of the Karman vortex street which persists as the primary feature of disturbance in the flow even in the turbulent regime. Compared with wall bounded flows, free shear flows are highly unstable due to the presence of inflection point in the velocity profile and the associated inviscid instability.

A weak wake is one wherein the minimum velocity is only 10% smaller than the maximum velocity, that is where the maximum defect of the velocity is around 10% of the free stream velocity. Different sizes of cylinders were tried in the turbulent channel and it was found that if the cylinder diameter d is large as compared to the channel width (e.g. d/h = 0.4) the Karman vortices help in quickly filling up the wake and even within a downstream distance of 10d, the wake ceases to exists.

When the cylinder diameter was d= 8mm, i.e. 10% of the channel width, a weak wake defined as above was obtained, which persisted for a long distance in the downstream direction. The experimental and the theoretical efforts in the present work was to study the stability of this wake to organised disturbances, and also study its capacity to sustain turbulence. Thus the propagation of organised disturbances along this wake was studied.

Nomenclature

C	Constant	h	Channel half width
Re	Reynolds number	R_{flow}	Flow Reynolds number
U_o	Centreline velocity	U	Instantaneous velocity
$\overline{U}$	Mean velocity	F_{11}	Longitudinal spectrum
F_{1R}	Cross-spectrum	$c=c_r+\imath c_i=\beta/\alpha$	Wave speed, complex
c_r	Wave speed, real	c_g	Group velocity
x	Down stream distance	$x^* = x/\sigma$	Normalised downstream distance
y	Distance across the channel from the wall		
u ,v, w	Velocity fluctuations		
$\hat{u}(y)$	Amplitude of fluctuation velocity from Orr-Sommerfeld (OS) solution		
$\tilde{u}$	rms velocity component due to organized disturbance		
U_{rms}	rms velocity of turbulence in the presence of cylinder		
U_{rmso}	rms velocity of turbulence in the absence of cylinder (free stream turbulence)		
$u_r = \sqrt{(U_{rms}^2 - U_{rmso}^2)}$	Excess rms velocity of turbulence in the wake		
σ	Half width of Gaussian distribution , distance from inflection point to centre of channel		
α	Wave number	$\beta = 2\pi f$	Circular frequency
$\beta = \beta_r + \beta_i$	Complex frequency		
μ	Dynamic viscosity	ρ	Density
θ	Phase angle	ψ	Disturbance stream function
ϕ	Amplification function of ψ	rms	Root mean square

2. Relevant Literature

The connection between stability theory and turbulent shear flow was first studied by Landau [1] based on a nonlinear stability model; however this model did not prove to be a suitable model for turbulence. Next, Malkus [2] studied the role of the turbulent mean velocity profile in the Orr-Sommerfeld equation. He proposed that if the mean velocity profile typical of wall-bounded turbulent flows is used in the solution of the classical Orr-Sommerfeld equation, then the profile would prove to be marginally or neutrally stable at the existing Reynolds number. Reynolds & Tiederman [3] proved that the Malkus theory was not valid by performing detailed calculations for a fully developed channel. Later on Reynolds continued work in the area of stability theory applied to fully developed wall turbulence along with Hussain, Hussain & Reynolds [4-5-6]. Initially they started with experiments by introducing controlled, weak, organised disturbances in a fully developed turbulent channel. Reynolds & Hussain [7] also did the theoretical investigations for this problem. Based on their three-way decomposition, they derived the disturbance equation as an extended Orr-Sommerfeld equation. However, neither theoretically nor

experimentally did they find any region of instability.

After Reynolds & Hussain, the problem was untouched for nearly thirty years. Sen & Veeravalli [8-9-10] studied this problem of relevance of hydrodynamic stability theory in understanding wall bounded flows, and they modelled the near wall region with anisotropy, and, theoretically they did observe the existence of Tollimen-Schlichting (TS)-like unstable modes. They found the region of instability to be outside the (stable) region of the theoretical and experimental results studied by Reynolds and Hussain [7], which is possibly why Reynolds and Hussain did not discover the unstable modes. Joshi [11] and Sen, Veeravalli & Joshi [12] compared the theoretical predictions of Sen et al [8-9-10] to their experiments using organised disturbances a fully developed turbulent channel and found that the results matched fairly well.

The works in the area of confined wakes are not many. Shair, Grove, Petersen and Acrivos [13] did experiments to study the effect of confining walls on the stability of a steady wake behind a circular cylinder and found that the stability is greatly enhanced with an increase of *d/h* from 1/20 to 1/5. Barkley [14] carried out a two-dimensional linear instability analysis for the mean flow in the wake of a circular cylinder and found that the eigen frequency of the mean flow tracks the Strouhal number of vortex shedding, almost exactly. The present work goes much beyond these results.

3. Objective and Methodology

The main objective of the present work was to study the evolution of organized disturbances in a weak confined wake both experimentally and numerically, with a view to elucidate the instabilities that arise in such a flow.

As mentioned above, the experiments were conducted in a rig specially designed to yield fully developed turbulent channel flow. Theoretical support for the results was provided by studying the stability of the confined wake profile using the standard Orr-Sommerfeld equation with the appropriate boundary conditions

Table 3.1: Typical flow parameters for the experiments

Centreline velocity	U_o	6.00 *m/s*
Channel half width	h	0.04 *m*
Reynolds Number, $\frac{U_o h}{\nu}$	Re	14,200

4. Experimental Setup and Instrumentation

A 2D turbulent channel (wind tunnel) of length 12.2 m and cross section 1.08 m x 0.08 m at the test section was used for the experiment. The walls (vertical) of the tunnel are made of 12 mm thick float glass. A plenum section consisting of several screens, a honeycomb, a 4.8:1 contraction and a small diverging section (to ensure rapid transition from laminar to turbulent flow) is present upstream of the test section. A more detailed description of the channel may be found in Joshi [11]. The organised disturbance is generated by a speaker and introduced into the flow through a slot of 1.5 mm width and 0.1m length, centred in the span-wise direction. The location of the slot was sufficiently downstream of the start of the test section to ensure the existence of fully developed turbulent channel flow. The schematic diagram of the setup and the coordinate system used are shown in figure 4.1. Typical flow parameters for the experiments are listed in Table 3.1.

The arrangement used to perturb the flow with a sinusoidal disturbance, without affecting the mean velocity profile in the wall region, is the same as that used by Joshi [11]. The speaker (ENBEE, 8Ω, 100W) was excited at the desired frequency using a function generator (Aplab, 1Mhz, Model: FG7MD). Velocity measurements were made with a hot-wire probe (Dantec 56C01; 5μm diameter Tungsten wire, approximately 1mm long) connected to an anemometer (TSI IFA 300). The output of the anemometer was suitably amplified and filtered before digitising using an a-to-d card (NI PCI 6143; 16bit) and then stored on a computer for processing. The output of the function generator was also digitised and stored to enable phase-locked averaging of the velocity signal.

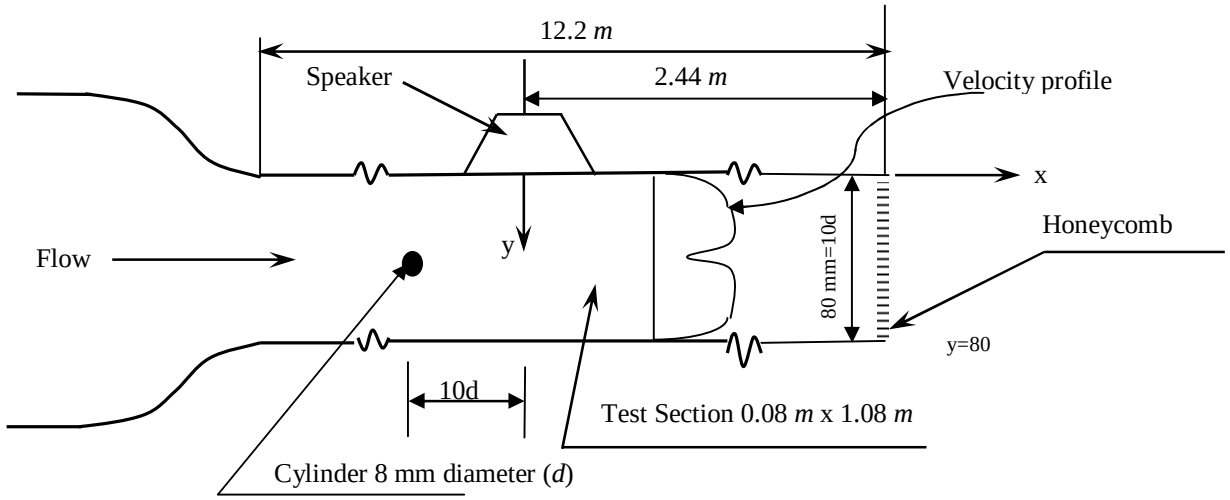

Figure 4.1: Definition sketch for the flow. The typical wake velocity profile and the coordinate system used are also shown.

5. Results and Discussion

5.1 Mean Velocity Profile

Measurements of the turbulent mean velocity profile in the wake region at different downstream distances from the cylinder are shown in Figure 5.1. The channel centerline velocity without the cylinder was approximately 6m/s. To account for minor changes in the ambient temperature and flow conditions, the profiles were scaled to match at one location (y=39mm). It is seen that all the profiles collapse well, indicating that the wake is virtually from $x = d$ to approximately $x = 20d$.

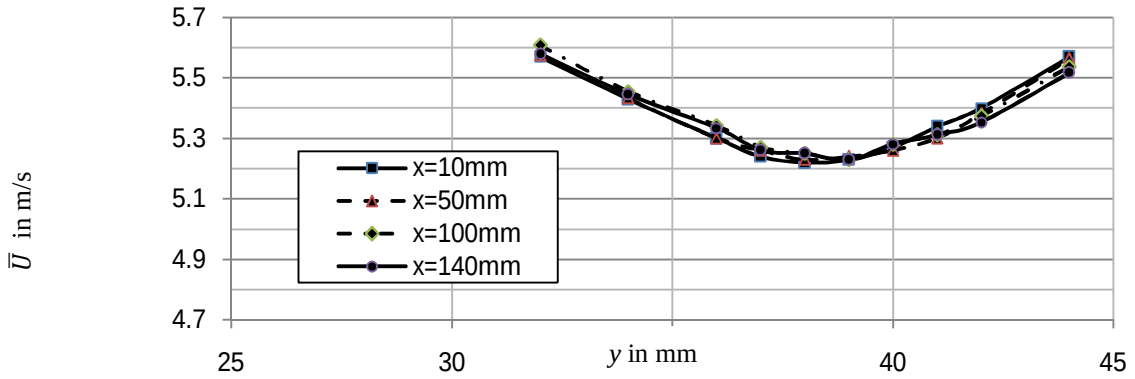

Figure 5.1: Experimental mean velocity profiles for various downstream distances, in the vicinity of the centreline.

The mean velocity profile obtained experimentally was modelled using a combination of parabolic and Gaussian profiles. The location of the inflection point was fixed by suitably selecting the standard deviation σ of the Gaussian distribution as shown in figure 5.2. In the present case σ=0.115, and figure 5.2 shows a perfect match of turbulent mean velocity profile and the synthesized mean velocity profile, in the wake region.

Theoretically, the mean velocity profiles for various downstream distances were obtained by spatial marching of the Navier Stokes equations with the theoretical mean velocity profile of wake. In this analysis the flow was assumed to be laminar. Figure 5.3 shows that the change in profile is insignificant.

The stability study focused on the wake region which is shown in solid line while, the rest is shown with a dotted line, in figure 5.2. For applying the boundary conditions the entire profile from wall to channel centre line is needed. The stability associated with the wake flow is an inviscid instability due to the presence of inflection point in the velocity profile, hence its shape outside central region is not important. Thus for the theoretical studies a combination of the Gaussian profile at the centre and the parabolic (laminar) profile elsewhere, is sufficient.

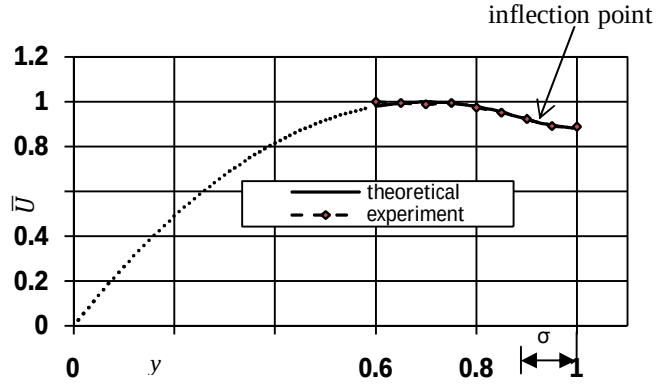

Figure 5.2: Modelling the experimental wake profile using a Gaussian profile (solid line) and a parabola (dotted line).

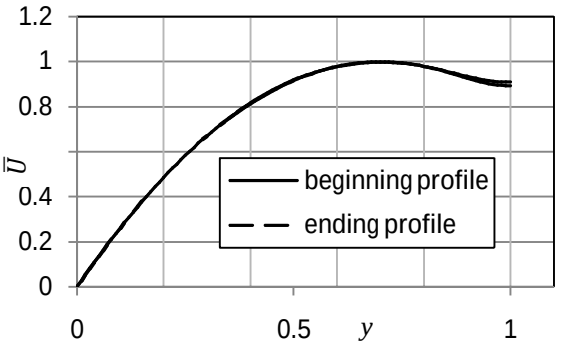

Figure 5.3: Theoretical mean velocity profiles from a calculation spanning the same downstream range as shown in figure 5.1 (i.e. 140mm).

5.2 Theoretical Formulations :-

In linear stability theory, developed by Tollmien and Schlichting, infinitesimal disturbances of a periodic nature are superimposed on the basic laminar flow and their growth rate, which is found to be exponential, is studied. For a primary flow parallel to the *x* direction, perturbations are assumed to be of the form

$$\psi = \phi(y)\, e^{i\alpha(x-ct)}. \qquad (5.1)$$

Where $c = \beta/\alpha$, and ψ is the complex disturbance stream function, $\phi(y)$ is the complex amplitude function, α is the spatial wave number, β is the frequency and c is the phase speed.

Inclusion of these perturbations in, and further linearization of the Navier Stokes equations gives the Orr-Sommerfeld equation (5.2) for the complex amplitude function ϕ . Generally, both α and c (or β) would have to be assumed complex implying that an amplitude growing both in space and time is to be considered.

$$i\alpha(\bar{u}-c)(\phi'' - \alpha^2\phi) - i\alpha\bar{u}''\phi - \frac{1}{Re}(\phi'''' - 2\alpha^2\phi'' + \alpha^4\phi) = 0 \qquad (5.2)$$

The synthesized profile for a weak wake was used in the Orr-Sommerfeld equation and numerically solved for eigenfunctions and eigenvalues to obtain decay/growth rates. The boundary conditions at the wall (y=0) are, $\phi = 0\,;\phi' = 0$ and at the channel centre (y=1) are: $\phi' = 0\,;\phi''' = 0,$ for the symmetric mode and $\phi = 0\,;\phi'' = 0$ for the anti-symmetric mode.

5.3 Turbulence measurements

Next we consider the turbulence levels in the confined wake, in the region where it does not spread. Figure 5.4 shows the turbulence levels (rms value) with and without the cylinder at x =10*d*. These have been denoted as U_{rms} and U_{rmso} respectively. It is observed from the figure that the turbulence level has gone up more than a factor of four when the cylinder is present. The peak excess turbulence level, u_r, due to the presence of the cylinder may be defined as $\sqrt{(U_{rms}^2 - U_{rmso}^2)}$. Figure 5.5 shows the evolution of u_r with the normalised downstream distance x^* ($x^* = x/\sigma$). It is seen from figure 5.5 that the excess turbulence level decays at an exponential rate.

5.4 Eduction of eigenfunction

2D organised disturbances at various frequencies like 300Hz, 200Hz, 100Hz and 50Hz were used to perturb the flow. The organised disturbance can be extracted from the background turbulence by averaging over a number of cycles at a given phase of the sinusoidal signal obtained from the function generator. While Joshi [11] reports good convergence of phase-locked averages for 10,000 cycles in the wall region, it is seen from Figure 5.6 that for the confined wake, even after 50000 cycles, full convergence has not been achieved. For comparison a pure sine wave is included in this figure.

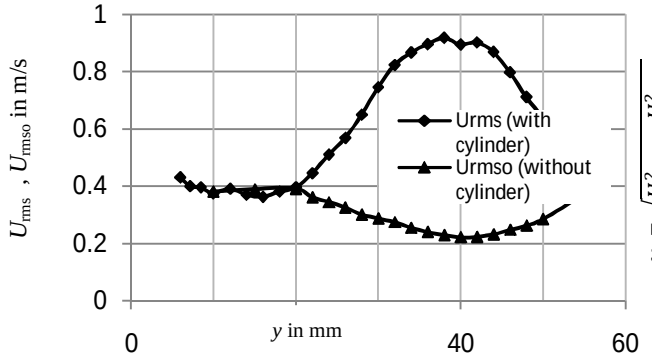

Figure 5.4: *Comparison of the turbulence levels with and without the cylinder at x/d = 10.*

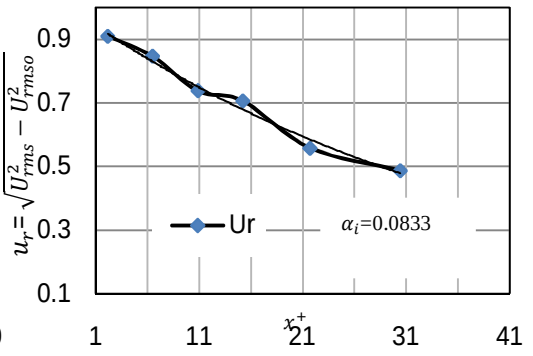

Figure 5.5: Evolution of turbulence excess velocity u_r

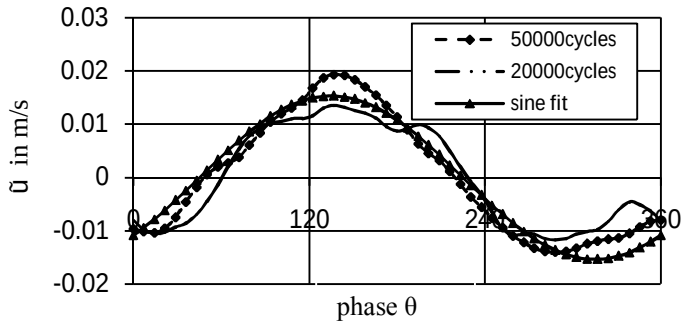

Figure 5.6: Comparison of phase averaging over different numbers of cycles. A pure sine wave is included for comparison.

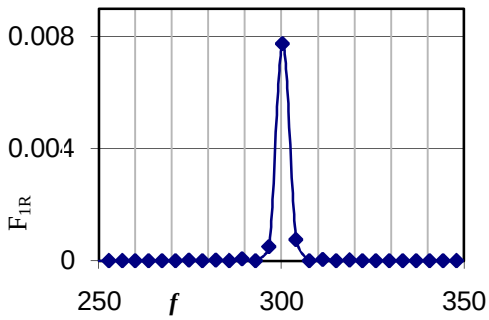

Figure 5.7: Absolute cross spectrum between the turbulence signal and the disturbance signal

One possible reason for this slow convergence is the jittering of mean velocity profile due to the Karman vortices. The presence of two inflection points, one on either side of the centreline also contributes to the problem. Waves originating from either side interfere with each other at a random phase difference and the resulting eigenfunction differs from cycle to cycle. Therefore 5 readings of 50000 cycles at each location were recorded and the average eigenfunction, $\tilde{u}$, was obtained from effectively 250,000 cycles. The average eigenfunction was also obtained from the cross spectrum between the turbulence signal and the disturbance signal. The cross spectrum plot in figure 5.7 shows a spike at the disturbance frequency. The area under the spike gives the magnitude of the eigenfunction, while the phase lag between the output of the function generator and the organised disturbance can be obtained from the imaginary part of the cross spectrum. Figure 5.8 shows a comparison between the eigenfunction obtained from phase locked averaging and the cross spectrum method. As can be seen the match is good.

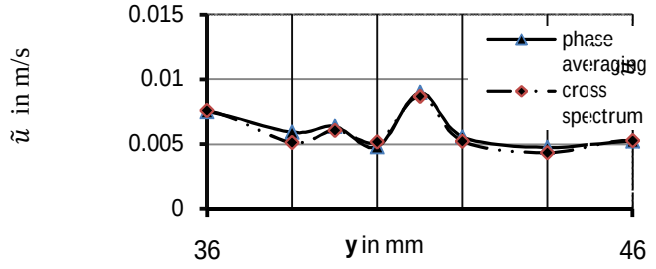

Figure 5.8: The eigenfunction obtained by phase locked averaging and the cross spectrum.

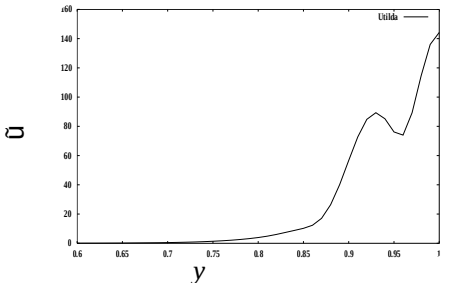

Figure 5.9: $\tilde{u}$ for the anti symmetric ϕ mode

Available online at www.sciencedirect.com

ScienceDirect

Procedia Engineering 00 (2015) 000–000

Procedia Engineering

www.elsevier.com/locate/procedia

5.5 Theoretical results

Figure 5.9 shows the anti symmetric mode obtained from the solution of the Orr-Sommerfeld equation.. The rms velocity $\tilde{u}_r$ is obtained as $\tilde{u}_r = \sqrt{2\phi'\bar{\phi}'}$. In figure 5.10 a comparison between the theoretically obtained eigenfunction and its experimental counterpart is shown. The match is good in the central region but the two curves diverge away from the centre. However in the important region (i.e. in the vicinity of the inflection point) the agreement is good.

The computations also indicate that the phase velocity c_r is nearly constant for all values of α, with $c_r \approx \bar{U}_i$ where, $\bar{U}_i$ is the mean velocity at the inflection point. Hence $c_r \approx c_g$ where c_g is group velocity. Hence the growth rate can be estimated as $-\alpha_i = \beta_i/c_r$.

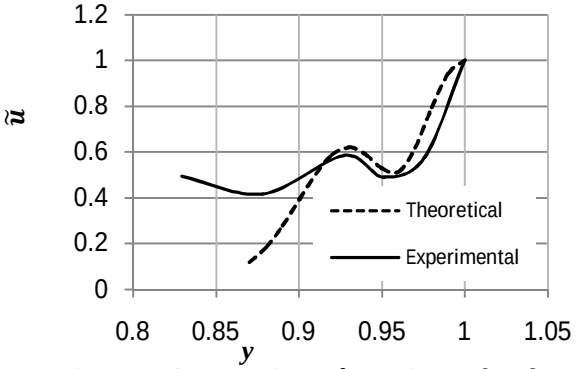

Figure 5.10 comparison of experimental and theoretical values of $\tilde{u}$

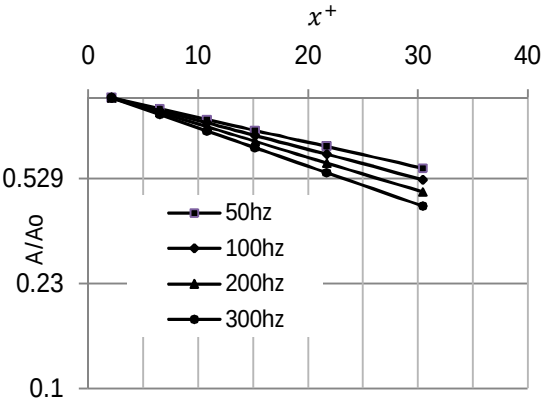

Figure 5.11: Evolution of the peak value of the eigenfunction . (Theoretical work.)

Figure 5.11 shows the theoretical results for disturbances of various frequencies. The evolution, of the peak amplitude of the eigenfunction, normalised by its initial value at x_o=10 mm (i.e. A/A_o), with the normalised downstream coordinate, x^*, has been shown. Note that $A/A_o = e^{-\alpha_i (x - x_o)}$, hence if the ordinate is shown on a logarithmic scale we expect to see straight lines at each frequency. This is what is observed, further the decay rate is higher at higher frequencies. All the modes obtained from the theoretical calculations were weakly damped at best.

5.6 Experimental Results

As mentioned earlier convergence in the experiments is very slow and hence our estimates of the eigenfunction is likely to possess large scatter. Figure 5.12 (a) shows a typical set of data points obtained for the experimental evolution of the peak ratio, $\tilde{u}/\tilde{u}_o$, along with their error bars. What is shown is the mean value bracketed by twice the standard error estimated. To within experimental error then the data support exponential decay. The data for disturbances at other frequencies shows similar scatter.

1877-7058 © 2015 The Authors. Published by Elsevier Ltd.
Peer-review under responsibility of organizing committee of the 6th BSME International Conference on Thermal Engineering (ICTE 2014).

Figure 5.12 (b) shows the evolution of $\tilde{u}/\tilde{u}_o$ for several different excitation frequencies. In this figure only the exponential fits are shown. The observation made in the discussion above, with the theoretical results, that the decay at higher frequencies is higher is verified by the experimental data, however, the corresponding decay rates are somewhat higher in the experiments. In Figure 5.12(b) the evolution of the excess turbulence and peak of the eigenfunction obtained without any external excitation, are also shown. The latter labelled 'Karman vortices' has been obtained by disconnecting the speaker but still using a sinusoidal signal of 165Hz (corresponding to the Strouhal frequency) to obtain phase locked averages. Both these data sets also support exponential decay, with the 'Karman vortices' set showing the highest decay rate. This is possibly due to the fact that no excitation was used and therefore in addition to a reduction in the strength of the disturbance there was a loss of coherence with the sinusoidal signal used for phase averaging also.

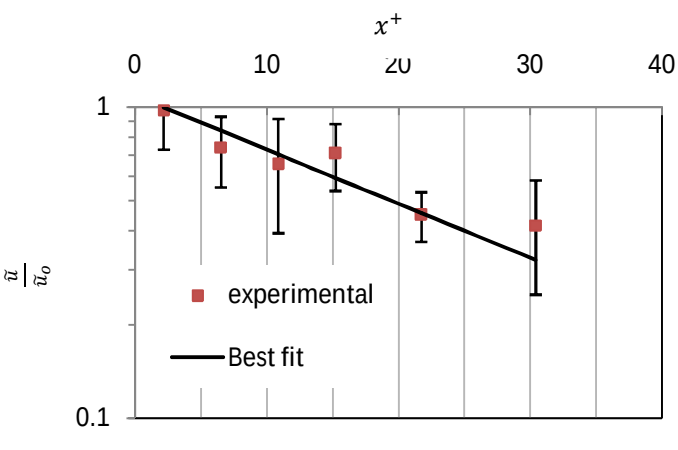

Figure 5.12(a): Variations of $\tilde{u}$ in downstream direction for 300Hz.

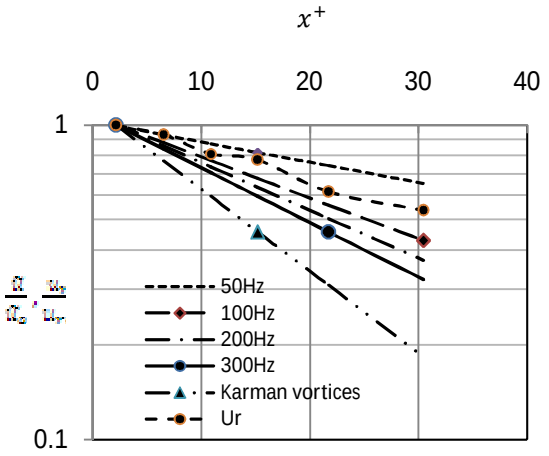

Figure 5.12(b): Variations of $\tilde{u}$ in downstream direction..

5.7 Spectral Analysis

Figure 5.13 shows power spectra of the longitudinal velocity (F_{11}) at centre of the channel for different downstream distances, without the sinusoidal perturbation. There is a spike seen at the Strouhal frequency (165 Hz) when the cylinder is present. The power spectrum plots also show that there is a decay of amplitude in the downstream direction.

From the power spectrum, for frequencies f= 50Hz, 100Hz, 200Hz and 300Hz, (corresponding to the different excitation frequencies) the corresponding densities were picked up and a best fit plot (similar to that of the eigenfunction peak) of the normalised excess spectral density $\frac{A-A_1}{A_o-A_1}$ versus x^+, (where A_o is the spectral density at the first location, x=10mm and A_1 is the value at x=10 mm when the cylinder is not placed) is shown in figure 5.14. These plots too are consistent with the earlier mentioned behaviour that higher frequencies decay faster.

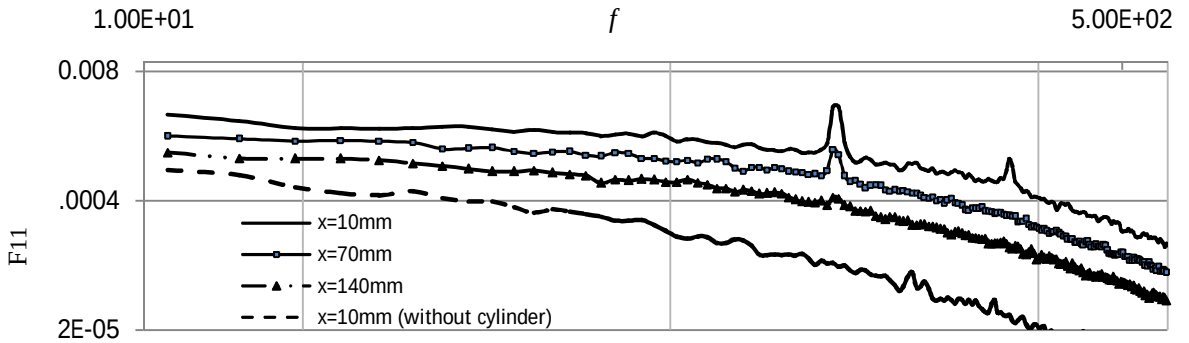

Figure 5.13: Power spectra with and without cylinder at different downstream distances, at y=40mm.

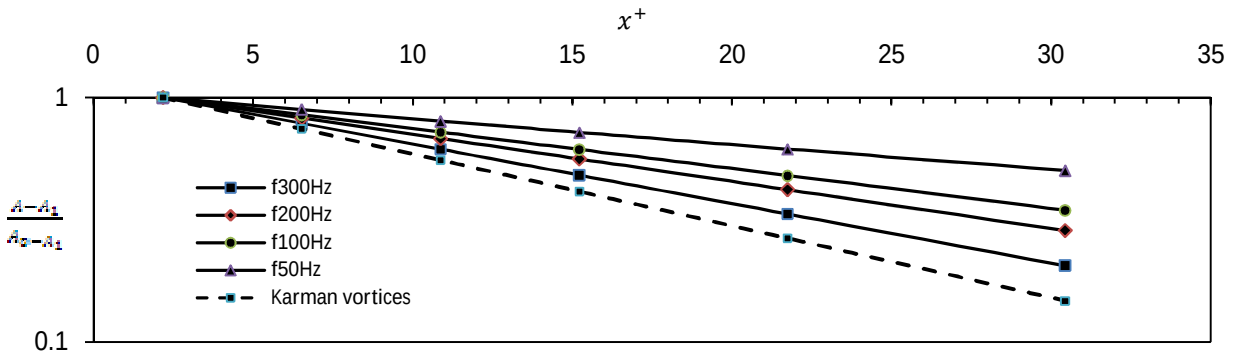

Figure 5.14: Evolution of the normalised excess spectral density in the downstream direction.

6. Conclusions

The mean velocity profile of the weak confined wake is virtually unchanged over a fairly large downstream distance ($x \approx d$ to $x \approx 20d$). Intriguingly this matches well with the theoretical evolution (laminar) wherein the background turbulence is ignored. Thus the confinement of the weak wake appears to exactly counter the spreading expected in the presence of the background turbulence.

The theoretical results indicate that although no unstable modes exist, weakly damped modes are present for a wide range of excitation frequencies. Moreover, the decay rate (exponential) increases with frequency. The theoretically obtained values of c_r are more or less constant and approximately equal to the mean velocity at the point of inflection. Hence, $c_g \approx c_r$, and the spatial growth rate may be obtained as $-\alpha_i = \beta_i / c_r$.

The experimentally determined eigenfunction matches the one obtained theoretically, quite well. Further, both the peak of the eigenfunction and the power spectral density excess exhibit exponential decay and show faster decay for higher frequencies. We note however, that the convergence of the experimental eigenfunction by phase averaging is extremely slow, possibly due to the interference of modes originating from the two inflection points.

7. References

[1] Landau L .D (1944) On the problem of Turbulence . C.R. Acad. Sci. U.R.S.S 44, 311-314.

[2] Malkus W. V. R., 1956, Outline of a theory of turbulent shear flow, *J. Fluid Mech.*, 1,521- 539.

[3] Reynolds W. C., and Tiderman W. G., 1967, Stability of turbulent channel flow, with application to Malkus's theory, *J. Fluid Mech.*, 27, 2, 253-272.

[4] Hussain A.K.M.F. and Reynolds W.C., 1970, The mechanics of an organized wave in turbulent shear flow, *J. Fluid Mech.*, 41, 2, 241-258.

[5] Hussain A.K.M.F. and Reynolds W.C., 1972, The mechanics of an organized wave in turbulent shear flow Part 2. Experimental results, *J. Fluid Mech.*, 54, 2, 241-261.

[6] Hussain A.K.M.F. and Reynolds W.C., 1975, Measurements in fully developed turbulent channel flow, *J. Fluids Eng.*, 97, 568-578.

[7] Reynolds W.C. and Hussain A.K.M.F., 1972, The mechanics of an organized wave in turbulent shear flow Part 3. Theoretical models and comparison with experiments, *J. Fluid Mech.*, 54, 2, 263-288.

[8] Sen P.K. and Veeravalli S.V., 1998, On the behaviour of organized disturbances in a turbulent boundary layer, *Sadhana*, 23, 167-193.

[9] Sen P.K. and Veeravalli S.V., 2000, Behaviour of organized disturbances in fully developed turbulent channel flow, *Sadhana*, 25, 423-437.

[10] Sen P.K., Veeravalli S. V., Carpenter P. W., Joshi G. and Josan P. S., 2007, Organised structures in wall turbulence as deduced from stability theory-based method, *Sadhana*, Vol. 32, Part 1 & 2, 51-64.

[11] Ganpati Narasimha Joshi., 2012, Experimental Investigation on the relevance of Hydrodynamic stability theory to wall-turbulence, Ph.D thesis, IIT, Delhi.

[12] Sen P.K., Veeravalli S. V., Joshi G.,2013, Stability theory and experiments in wall-turbulence, Procedia Engineering 56 (2013), pp. 29-38.

[13] Shair F. H., Grove A. S., Petersen E.E. and Acrivos A (1963) The effect of confining walls on the stability of the steady wake behind a circular cylinder, *J. Fluid Mech.*, 17, 4, 546-550.

[14] Barkley D (2006) Linear analysis of the cylinder wake mean flow .Euro physics letters 75(5) 750-756.